NTNU – Trondheim
Norwegian University of
Science and Technology

Fuel-Efficient Control Allocation for Supply Vessels

Kjell Erik Larsen

Master of Science in Engineering Cybernetics
Submission date: June 2012
Supervisor: Thor Inge Fossen, ITK
Co-supervisor: Ivar Ihle, Rolls Royce

Norwegian University of Science and Technology
Department of Engineering Cybernetics

NTNU
Norwegian University of Science and Technology

Faculty of Information Technology, Mathematics and Electrical Engineering
Department of Engineering Cybernetics

MSC THESIS DESCRIPTION SHEET

Name:	Kjell Erik Larsen
Department:	Engineering Cybernetics
Thesis title (Norwegian):	Drivstoffoptimal pådragsallokering for forsyningsskip
Thesis title (English):	Fuel-Efficient Control Allocation for Supply Vessels

Thesis Description: The purpose of the thesis is to design a control allocation system for dynamic positioning (DP). Thrust losses must be considered when designing the thrust allocation algorithms in order to avoid stability problems. Implement the control allocation system on CyberShip 3, which is a scale model of a supply vessel.

The following items should be considered:

1. Define the scope of the thesis and clarify what your contributions are.
2. Give an overview of the literature on control allocation.
3. Design an optimal control allocation scheme for use in DP. Use the model of CyberShip 3 and a DP control system for verification and testing.
4. Suggest a set of suitable criteria to evaluate the performance of the control allocation system.
5. Run experiments in MCLab to verify the design in a practical situation.
6. Conclude your results.

Start date:	2012-01-23
Due date:	2012-07-13

Thesis performed at:	Department of Engineering Cybernetics, NTNU
Supervisor:	Professor Thor I. Fossen, Dept. of Eng. Cybernetics, NTNU

Acknowledgements

This thesis is the result from my work conducted from January 2012 to June 2012. The work has been carried out at the Department of Engineering Cybernetics at Norwegian University of Science and Technology.

Most of all, I would like to thank my supervisor Thor Inge Fossen at the Department of Engineering Cybernetics and Centre for Ships and Ocean Structures (CeSOS) at NTNU. His support, good guidance and enthusiasm for marine control systems has inspired me in this thesis.

A personal graditude and thanks goes to my friend Willy Kristiansen for his help with experimental testing during the nights. And for his funny remarks during stressful times. I would also give a personal thanks to Torgeir Wahl at the Department of Marine Technology for all his help in the MCLab with Cybership III. His knowledge of the Cyberhsip III and the equipment at the Marine Cybernetics Lab. Without his help the testing of Cybership III in the Marine Cybernetics Lab would not be possible. A thanks goes also to my friend Svein Ollestad for helping me with last minute structure check.

To last I would like to express my deepest gratitude to my family, Trond-Eivind Larsen, Marianne Helland, Eivind Larsen and Espen Larsen for their continuous support these last five years of study. Without their love and unconditional support the world would be a more grim place.

Trondheim, Norway
July 2012 Kjell Erik Larsen

Abstract

The motivation behind this thesis was to find a control allocation algorithm to reduce the power consumption onboard maritime vessels. As more and more maritime operations starts to go at deeper sea levels the further away from the shore the maritime vessels goes. The need to reduce power consumption to be able to operate at a longer time period out in the sea can save maritime businesses for increased costs during missions a deeper sea levels.

To reduce power consumption onboard a typical supply vessel used in the North Sea a power efficient control allocation method was designed. A simulation model was designed to be able to test the efficiency of such a control allocation method. Conditions such as wind, current and waves were modelled using standard models for North Sea conditions. A typical model for vessel dynamics were modelled to be able to see the effect of the environmental loads acting on supply vessel. Thruster dynamics such as losses and characteristics during were added for a more realistic condition onboard the vessel. Inflow velocity into the propeller blades were simulated as this reduces the potential thrust production able at a certain shaft speed. Realistic rate in which the propellers could rotate were added. As the inflow into the propeller blades effects the efficiency of the thruster, the control allocation method was designed to reduce the possibility of one thruster to interact with another thruster by avoiding water flow from one thruster into the other thruster. The control allocation method was thus designed with several thrust production zones. Each of these sectors were monitored by using a supervisor to find the most power-efficient sector. To reduce power usage within each sector, the control allocation used each thrusters thrust-to-power relation to evenly distribute the power amongs the avaiable thrusters onboard the supply vessel. The control allocation method would then reduce the use of thrusters with poor thrust-to-power relation by using the ones with better relation. If one thruster has high power consumption, the idea behind the control allocation method would be to redistribute this produced thrust to the other thrusters avaiable. This was only done if the required force calculated by the controller was obtained.

The method designed was a supervisory control allocation as described in chapter 4. It was shown in the Simulation Cases 1-2 that the power was minimized by still regaining the desired position of the supply vessel. If a more power-efficient sector was found on the other side of a forbidden thrust production zone, the thrusters would swipe through this zone as fast a possible. This was confirmed experimentally in the MCLab at MarinTek at NTNU. The bau azimuth onboard the supply vessel used, had a very poor thrust-to-power relation compared to the stern pods. This bau azimuth was rarely used due this relation, and was only used if necessary, and was confirmed both in the simulation cases and experimentally. The supervisory control allocation method was confirmed to be much more power-efficient compared to a explicit control allocation method in the simulation study. This showed the potential of the supervisory control allocation method to obtain a much better solution compared to other traditional solutions of the control allocation problem.

Sammendrag

Motivasjonen bak denne oppgaven var å finne en kontroll tildelingsalgoritme for å redusere strømforbruket ombord maritime fartøy. Ettersom flere og flere maritime operasjoner begynner å gå på dypere havnivået jo lenger vekk fra kysten kommer de maritime fartøyene. Behovet for å redusere strømforbruket for å kunne operere på en lengre periode ute i havet kan spare maritime bedrifter for økte kostnader på oppdrag i dypere havnivå.

For å redusere strømforbruket om bord en typisk forsyningsfartøy brukt i Nordsjøen ble en energieffektiv kontroll allokeringsmetoden laget. En simuleringsmodell ble utviklet for å kunne teste effektiviteten av en slik kontroll tildelingsmetode. Forhold som vind, strøm og bølger ble modellert ved hjelp av standard modeller for forholdene i Nordsjøen. En typisk modell for fartøyets dynamikk ble modellert for å kunne se effekten av de miljøbelastninger som virker på ett forsyningsskip. Thruster dynamikk som tap og karakteristikk ble laget for en mer realistisk tilstand av fartøyet. Innstrømings hastighet inn til propellbladene var simulert, som reduserer potensialet for skyvekraft for en viss aksel hastighet. Realistisk rotasjonshastighet for propellene ble lagt til. Ettersom innstrømingnen inn til propellbladene reduserer effektiviteten til thrusteren, ble kontroll tildelingsmetode for å redusere muligheten for en thruster å forstyrre med en annen propell utviklet ved å unngå vannstrømmen fra en propell inn til den andre thruster. Kontrollen tildelingsmetoden ble således utformet med flere tillate skyvekraftssektorer. Hver av disse sektorene ble overvåket ved hjelp av en veileder for å finne den mest strømgjerrige sektoren. For å redusere strømforbruket innenfor hver sektor, brukes kontrollentildelingen hver thrustere sin skyvekraft-til-effekt forhold for å fordele effekt mellom de tilgjengelige thrusterene ombord på forsyningsskipet. Kontrollen tildelingsmetoden vil da redusere bruken av trustere med dårlig skyvekraft-til-effekt forhold ved å bruke de med bedre forhold. Dersom en thruster har høyt strømforbruk, ville ideen bak kontrollen tildelingsmetoden være å omfordele denne produserte skyvekraften til de andre thrustere som er tilgjenngelige. Dette ble bare gjort hvis den nødvendige kraften beregnes av kontrolleren ble oppnådd.

Metoden konstruert var en veiledende kontroll allokeringsmetode som beskrevet i kapittel 4. Det ble vist i simuleringen test 1-2 at effekten ble minimert med fortsatt å gjenvinne ønsket posisjon forsyningsskip. Hvis en mer energieffektiv sektor ble funnet på den andre siden av en forbudt skyvekraftssone, ville thrusterne sveipe gjennom denne sonen så fort en mulig. Dette ble bekreftet eksperimentelt i MCLab ved Marintek ved NTNU. Den fremre azimuthen ombord brukt i forsyningsskipet hadde en veldig dårlig skyvekraft-til-effekts forhold i forhold til de bakre podene. Dette fremre azimuthen ble sjelden brukt pga dette forholdet, og ble bare brukt om nødvendig, dette ble bekreftet både i simuleringen testene og eksperimentelt. Kontrollen tildelingsmetoden ble bekreftet å være mye mer energieffektiv enn en eksplisitt kontroll tildelingsmetode i simuleringen studiet. Dette viste potensialet for veiledende kontroll tildelingsmetode for å oppnå en mye bedre energi løsning i forhold til andre tradisjonelle løsninger av kontroll tildeling problemet.

Contents

List of Figures

List of Tables

Chapter 1

Introduction

1.1 Motivation

In today's global activities maritime vessels play an important role. From transportation of goods and passengers to operations in the oil and gas industry. The different roles for maritime vessels in these types of industries have given a great advancement in maritime operations and designs. Designs such as the vessels in particular and in the software they use. The increase of oil and gas demands has led to a significant increase of the use of Dynamic Positioning (DP) and thruster assisted Position Mooring systems.

As the operations of marine vessels goes into deeper and deeper water and further away from the coast line, the demand for more fuel-efficient solutions becomes more important. This is the motivation behind this thesis. In this thesis a fuel efficient control view is taken, especially when it comes to control allocation.

1.2 Control System Structure

The typical control system overview can be seen in Figure 1.1. The control system is assumed to be well known and parts of it will be discussed later. The subject of this paper is the Thrust/Control Allocation and will be discussed in section 1.3.

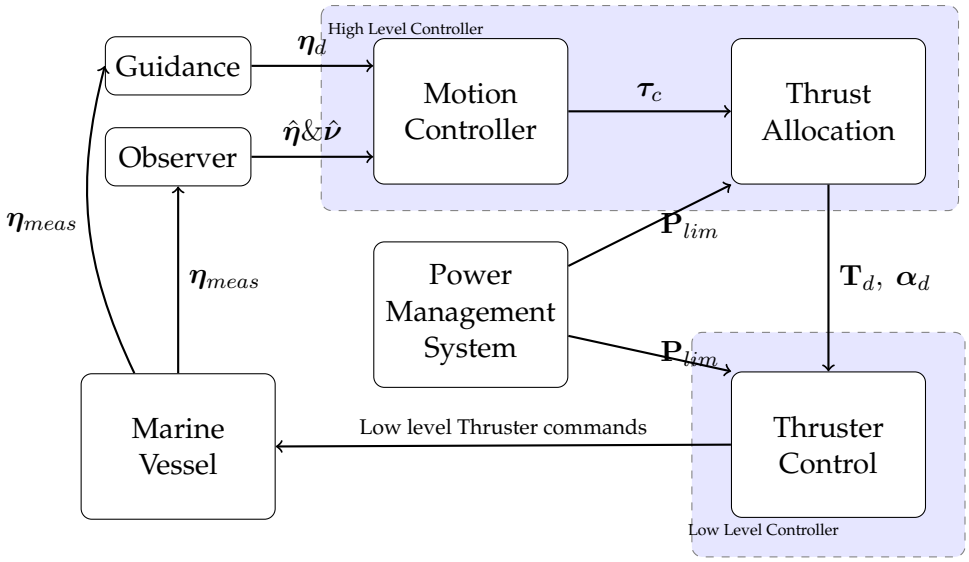

Figure 1.1: Control System overview

The set points such as the desired propeller thrust T_d from the Thrust Allocation is often mapped from thrust to shaft-speed in the low-level controller before the required engine torque is calculated. Example of such mappings can be found in Appendix A.3.1. The torque setpoint / shaft speed setpoint is then sent to the propulsion units (in the Marine Vessel block). The propulsion units driven by the low-level controller can be divided up as seen in Figure 1.2.

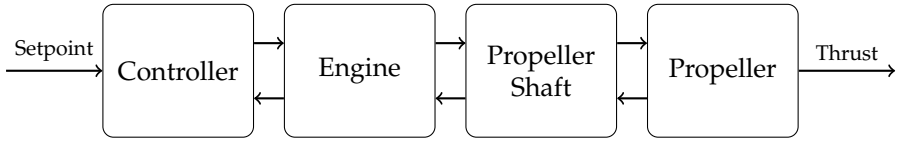

Figure 1.2: Propulsion units block diagram

1.3 Control Allocation

The thrust allocation problem can be viewed in the Figure 1.3 below. The problem is how to distribute the commanded generalized force, $\boldsymbol{\tau}_c$, computed by the motion controller. The thrust allocation problems task is to compute the desired thrust force and direction of each thruster and rudder onboard the vessel. This normally rises to a optimization problem as the thrusters cannot produce infinite thrust.

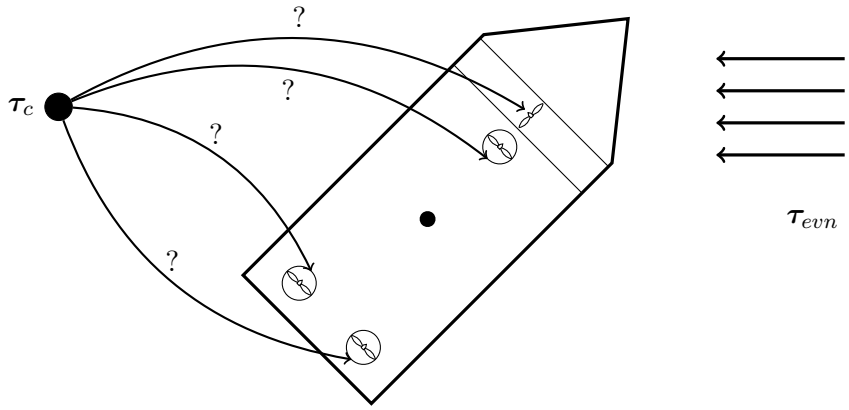

Figure 1.3: Thrust Allocation Problem

An overview of control allocation within the aerospace community can be found in Oppenheimer et al. (2010) and a good maritime application overview can be found in Fossen and Johansen (2006).

The main goal of the control allocation problem is to keep the error between the commanded generalized force $\boldsymbol{\tau}_c$ and the allocated force $\boldsymbol{\tau}_d$ as small as possible. This can be written as the error $\boldsymbol{e} = \mathbf{B}(\boldsymbol{\alpha}_d)\mathbf{T}_d - \boldsymbol{\tau}_c$. Where $\mathbf{B}$ is the thruster configuration matrix determined by the location

and direction of each individual thruster and rudder, as explained (as $\mathbf{T}(\boldsymbol{\alpha})$) in Fossen (2011). The variable $\boldsymbol{\alpha}_d$ is the desired thruster and rudder angles calculated by the control allocation problem. Likewise $\boldsymbol{T}_d$ is the desired forces from the thrusters and rudders from the allocation problem.

The control allocation problem is typically a iterative optimization problem where the error between the generalized forces from the controller and control allocation is minimized. However explicit solutions such as use of pseudo-inverse exist.

Control allocation solutions depend entirely on the available data and constraints (Hardware and Software). For example in the case of integration of the Power Management System (PMS), power spikes might be considered to be crucial to prevent. In such cases rapidly changing the propeller shaft speed might be unwanted. The same criteria might be unwanted in the case of preventing wear and tear of the motor. These are just some examples of the difficulty of integrating a control allocation towards a fully operational vessel.

The control allocation is quite often designed in a modular case. This simplifies the design choices for the different functionalities of the total control system onboard vessels. With modular design the motion controller is simplified as it has no information of the details of the control allocation.

When designing a control allocation scheme some choices must be made towards maneuverability, power-efficiency and wear-and-tear. Specific solutions weights between these options. In the case of power-efficient solutions a optimal solution might be to align the thrusters towards the mean environmental forces, however in the case of sudden forces acting perpendicular to the direction of the thrusters the ship might get out of position. This is called a singular solution. To increase maneuverability a non-singular solution might be considered. However such a non-singular solution is not as power-efficient as a singular solution. In these cases there are a trade-off between having the best maneuverability and the best power-efficient solution.

1.3.1 Previous Solutions

Maritime solutions to the control allocation can be divided into two main classes, linear and non-linear models respectively. These groups have two subgroups: unconstrained and constrained allocation.

Commonly in control allocation algorithm there is a linear model

$$\boldsymbol{\tau_d} = \mathbf{B}\boldsymbol{u} \tag{1.1}$$

between the desired generalized force $\boldsymbol{\tau_d}$ and the control inputs $\boldsymbol{u}$ from the control allocation algorithm. These control inputs commonly contains the desired thrust $\mathbf{T}_d$, angle of thrusters or rudders $\boldsymbol{\alpha}_d$ and slack variables $\mathbf{s}$. The matrix $\mathbf{B}$ describes the relationship between the control inputs $\mathbf{u}$ and the desired generalized force $\boldsymbol{\tau_d}$.

In Bodson (2002) there is a comprehensive comparison between several state-of-the-art linear control allocation methods. And one of the conclusions is that the optimization-based methods tend to outperform alternative methods in the literature in areas such as minimizing the control effort and unnecessary infeasibility. Quadratic formulations also seems favorable compared to the linear formulations as the quadratic methods tens to combine the use of all control surfaces, Petersen and Bodson (2006). While the ∞-norm formulations minimizes the maximum effector use and thus lead to a more balanced use of effectors, which has advantages for robustness to failures and nonlinearities (Frost et al. (2009), Frost and Bodson (2010), Bodson and Frost (2011)) .

Unconstrained Linear Control Allocation

If any constraints are neglected on the virtual control inputs $\mathbf{u}$, a control allocation algorithm can be stated as a weighted least-squared problem follows

$$\min_{u \in \mathbb{R}^p} = \frac{1}{2}(\boldsymbol{u} - \boldsymbol{u}_{pref})^T \mathbf{W}(\boldsymbol{u} - \boldsymbol{u}_{pref}) \tag{1.2a}$$

subject to

$$\boldsymbol{\tau_c} = \mathbf{B}\mathbf{u} \tag{1.2b}$$

where $\mathbf{u}_{pref}$ is the preferred value of $\mathbf{u}$ and $\mathbf{W} \in \mathbb{R}^{p \times p}$ is a positive definite weight matrix. The weight matrix is often chosen to be diagonal with positive elements to create a positive definite matrix. Equation (1.2) is however nonlinear, but an explicit solution can be found if $\mathbf{B}$ has full rank. If $\mathbf{B}$ has full rank the Lagrange multipliers can be used to derive a generalized inverse matrix $\mathbf{L}$. An explicit linear solution can then be found as

$$\mathbf{u} = \mathbf{u}_{pref} + \mathbf{L}\boldsymbol{\tau_c} \tag{1.3a}$$

$$\mathbf{L} = \mathbf{W}^{-1}\mathbf{B}^T(\mathbf{B}\mathbf{W}^{-1}\mathbf{B}^T)^{-1} \tag{1.3b}$$

For discussion and examples of use of the generalized inverse, please see Bordignon and Bodden (1995), Virnig and Bodden (1994), Enns (1998), Snell et al. (1990), Durham (1993), Oppenheimer et al. (2010) and Fossen and Sagatun (1991).

If $\mathbf{W} = \mathbf{I}$ and $\mathbf{u}_{pref} = 0$ the explicit solution can be found by the Moore-Penrose pseudo inverse, Horn and Johnson (1985) and Golub and van Loan (1983), as follows:

$$\mathbf{u} = \mathbf{B}^+\boldsymbol{\tau}_c = \mathbf{B}^T(\mathbf{B}\mathbf{B}^T)^{-1}\boldsymbol{\tau_c} \tag{1.4}$$

where then $\mathbf{B}^+$ is the Moore-Penrose pseudo-inverse matrix.

If $\mathbf{B}$ does not have full rank, i.e it is not possible to produce any commanded generalized force $\boldsymbol{\tau}_c$, it is possible to use a damped least-square pseudo-inverse, Golub and van Loan (1983)

$$\mathbf{L}_\epsilon = \mathbf{W}^{-1}\mathbf{B}^T(\mathbf{B}\mathbf{W}^{-1}\mathbf{B} + \epsilon\mathbf{I})^{-1} \tag{1.5}$$

where $\epsilon \geq 0$ is the regulation parameter, which should be small. In the case if $\mathbf{B}$ has not full rank, ϵ must be strictly positive. It is also possible to achieve explicit solution to the control allocation problem by using singular value decomposition (SVD) with or without $\mathbf{B}$ having full rank, Golub and van Loan (1983) and Oppenheimer et al. (2010) respectively.

Constrained Linear Control Allocation

If there is any saturations on the virtual control input $\boldsymbol{u}$ it has been shown in Durham (1993) that no single generalized inverse can be found to

calculate the exact control allocation solution. However, it is possible to use the redistributed pseudo-inverse method along with projecting the virtual control input onto a saturated set (see e.g. Virnig and Bodden (1994) and J.P. Shi and Liu (2010)). This type of solution does not guarantee that a feasible solution can be found. Examples where it still can give results are given in Bodson (2002).

Besides explicit solutions to solve linear control allocation there are some iterative solutions to the control allocation problem. These algorithms uses an iterative linear program, where both the cost functions and the constraints are described with linear equations respectively. The cost function is often described either the 1-norm or ∞-norm. In Linear Programming syntax the cost function is described by $J = \mathbf{c}^T\mathbf{x}$, where $\mathbf{x}$ is the virtual control inputs and $\mathbf{c}$ the weights. A linear control allocation algorithm with for example the 1-norm can be written as follows

$$\min_{u,s} \quad \sum_{i=1}^{p} w_i \left|u_i\right| + \sum_{j=1}^{m} q_i \left|s_i\right| \tag{1.6a}$$

subject to

$$\mathbf{Bu} + \mathbf{s} = \boldsymbol{\tau}_c \tag{1.6b}$$

$$\mathbf{u}_{min} \leq \mathbf{u} \leq \mathbf{u}_{max} \tag{1.6c}$$

$$\Delta\mathbf{u}_{min} \leq \mathbf{u} - \mathbf{u}_{prev} \leq \Delta\mathbf{u}_{max} \tag{1.6d}$$

where $\boldsymbol{s}$ is the slack variable to ensure that the equality constraint (1.6b) always has an solution even though the virtual control inputs cannot fulfill $\mathbf{Bu} = \boldsymbol{\tau}_c$. The slack variables are normally weighted much higher than the virtual control inputs, this is to ensure the solution is close as possible to the commanded generalized forces. Examples of implementation of linear control allocation schemes can be found in Bodson (2002), Lindfors (1993) and Bodson and Frost (2011). One thing that should be noted with using linear control allocation is that it does not ensure that a global solution can be found, only guaranteed local solutions can be found (Nocedal and Wright, 2006). This can be viewed in the 2-dimensional example Figure 1.4 below using Linear Programming syntax $\mathbf{c}^T\mathbf{x}$.

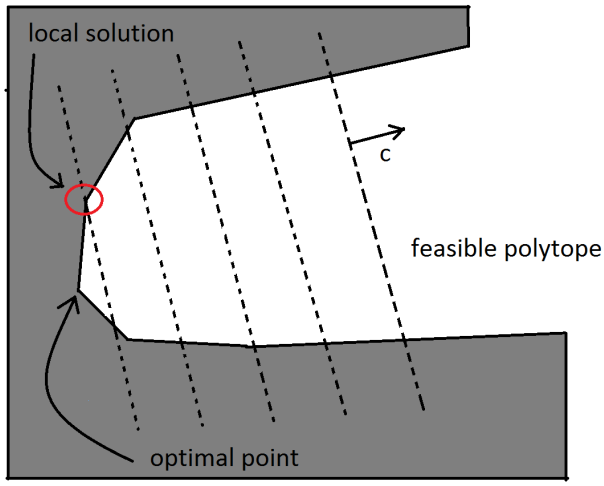

Figure 1.4: 2D linear optimization example

The effectiveness of the solver is also highly dependent on solver. In the case of the much used Simplex method it is very efficient, but has a poor worst-case performance, Nocedal and Wright (2006). In Lindfors (1993) the nonlinear relationship between the thrust and angle of the azimuth thruster ($Tx = Tcos(\alpha)$ and $Ty = Tsin(\alpha)$) was linearised using an octagonal polytope giving a slight error. However when the solution was in one of the corners of the polytope this lead to less chattering in the azimuth angle as the algorithm required less thrust to change the azimuth angle. Using this Lindfors (1993) rotated previous solutions to always lie in one of the corners of the polytope to decrease azimuth chattering. The idea behind this can be seen in Figure 1.5. Less azimuth chattering results in less mechanical movement and thus reduces the wear-and-tear of the mechanical system.

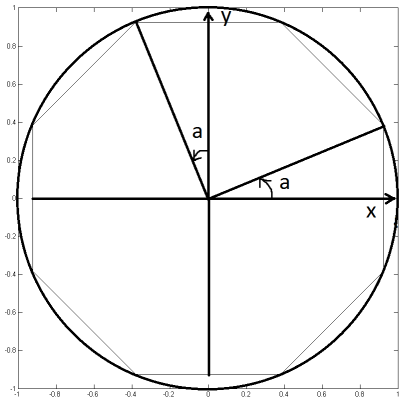

Figure 1.5: Proposal starting point for linear programming with new coordinate system used in Lindfors (1993)

Linear Quadratic Control Allocation

One of the most used algorithms types in maritime control allocation is a linear quadratic control allocation also known as a Quadratic Programming solver (QP-solver) . These algorithms use the 2-norm in the cost function while the constraints are linear, such as the equation (1.2). A linear 1-norm is also typical in some algorithm solutions. The benefit of a QP-solver is that the global solution is found within the specified region, which must be convex, and it is guaranteed that a solution is found or that the problem is infeasible, Nocedal and Wright (2006). However as with the Linear Programming there are no guarantees on how many iterations the solver will use. Standard QP-solver can be written as follows

$$\min_{\mathbf{x}} \frac{1}{2}\mathbf{x}^T\mathbf{H}\mathbf{x} \tag{1.7a}$$

subject to

$$\mathbf{A}_{eq}\mathbf{x} = \mathbf{b}_{eq} \tag{1.7b}$$

$$\mathbf{A}\mathbf{x} \leq \mathbf{b} \tag{1.7c}$$

where $\mathbf{x} = [u, s]^T$. The weight matrix $\mathbf{H}$ must be strictly positive. $\mathbf{A}_{eq}$ and $\mathbf{A}$ is the equality and inequality matrices respectively. And similar the $\mathbf{b}_{eq}$ and $\mathbf{b}$ is the equality and inequality constraints. The 1-norm can easily be added to (1.7a) by $\mathbf{g}^T\mathbf{x}$.

- Unconstrained Linear Quadratic Control Allocation

Unconstrained linear quadratic algorithms are proposed by Sørdalen (1996, 1997a,b), Berge and Fossen (1997) and Garus (2004). Singularity avoidance is added in Sørdalen (1996, 1997a,b) and Berge and Fossen (1997), and even though the algorithm is unconstrained, infinity thrust is avoided in singularity cases. In Sørdalen (1997b) a proposal to solve the problem with thruster capable to produce thrust in negative and positive direction. In Sørdalen (1996, 1997a,b) the extended thrust vectors $Tx = Tcos(\alpha)$ and $Ty = Tsin(\alpha)$ are used to find the direction of the thrust and afterwards low pass filtered. The filtering of the thruster direction reduces also the chattering which will reduce mechanical wear and tear. The singularity avoidance is achieved by using to previous thrust direction to modify the singular value decomposition used in the thruster forces calculation. Berge and Fossen (1997) the low pass filtered desired generalized force are used to calculate the thrust direction. The singularity avoidance is achieved by using a damped least squares method from the previous thrust direction in the calculation of the thruster forces. Garus (2004) includes different solutions with fixed thrusters by using quadratic thrust allocation, and also includes how to take into account a failure of one of the thrusters.

- Constrained Linear Quadratic Control Allocation

The literature is full with utilization of constrained linear quadratic control. Some of the typical objectives and constraints found in the literature is the following

- Maximum thrust production limitation for each thruster due mechanical limitations such as maximum shaft speed.
- Rate constraints on both azimuth angles and thrust due to mechanical limitations.

- Maximum allowed power drainage due to generator specifications and number of generators active on the power bus connection to the propulsion units. Minimization power spikes and spike amplitudes might also be considered, reducing effectiveness to change thrust abruptly. Spikes in power might also lead to blackout onboard the vessel, which leads to total loss of producing any form of thrust.
- Minimization of fuel consumption as an objective.
- Minimization of wear-and-tear as this can lead to reduced efficiency of produced thrust. Wear-and-tear can then lead to mismatch between parameters used in the control allocation algorithm and the mechanical system of the thrusters.
- Handle thruster failures with some sort of failure tolerance.
- Forbidden thrust production zones might be wanted to reduce thruster losses (See Appendix A.3.2)

Methods and algorithms for handling these types of constraints and objectives can be found in e.q. Fossen (2011), Johansen et al. (2003, 2005, 2008), Swanson (1982), Lindegaard and Fossen (2003), Ruth et al. (2007); Ruth and Sørensen (2009); Ruth et al. (2009), Jenssen and Realfsen (2006).

In Johansen et al. (2003, 2005, 2008) the problem is solved by multiparametric quadratic programming leading into piecewise linear functions. Rudder dynamics is also included in these methods. The problem is solved in real time by precomputing the piecewise linear functions. Johansen et al. (2005) solves the problem for fixed thruster direction only. While Johansen et al. (2003, 2008) solves the problem with rotation thrusters in a nonconvex region. The nonconvex region is decomposed into convex regions to be able to solve it using a multiparametric-QP algorithm. Lindegaard and Fossen (2003) solves the thrust allocation problem with constraints on one thruster only.

In Sørensen and Adnanes (1997) the interaction between the control allocation and the low level thrust controller has been studied. This interaction is particularly important in extreme seas where the propeller losses can be quite large due to ventilation and in-and-out-of-water effects (See Appendix A.3.2) and may lead to propeller spin Øyvind

N. Smogeli et al. (2008). In Ruth et al. (2009) a control allocation method is proposed to reduce propeller spin in case of ventilation and in-and-out-of-water effects by using ventilation detection described in Øyvind N. Smogeli et al. (2008) to reallocate forces to non-ventilated thrusters.

Jenssen and Realfsen (2006) describes a practical strategy for optimal thrust allocation in terms of power generations constraints. This is done by balancing the load on different power buses and switch boards.

Ruth et al. (2007); Ruth and Sørensen (2009) are discussed later in Chapter 4.

Constrained Nonlinear Control Allocation

Nonlinear control allocation in the literature can be found e.q. Sinding and Anderson (1999), Webster and Sousa (1999), Liang and Cheng (2004), Johansen (2004), T. A. Johansen and Berge (2004), and Tjønnås and Johansen (2005, 2007).

1.4 Thesis Outline

The thesis is outline as follows

Chapter 1 Introduction

- Motivation
- Control Allocation Introduction
- Literature on Control Allocation

Chapter 2 CyberShip 3

- Quick overview of CyberShip 3
- Key features offering in software associated with CyberShip 3

Chapter 3 Cybership 3 modelling

- Contrains modelling of the kinematics and kinetics of the CyberShip 3. Environmental models for vessel loads are included, and modelling of the propulsion units onboard Cybership 3.

Chapter 4 Control Allocation

- Introduction
  - General introduction of Quadratic programming used in Control Allocation
- Stepwise modelling of the supervisory control allocation method.

Chapter 5 Simulation Study

- The simulation study includes an open loop solution, full sea state simulation testing and singularity avoidance testing of the implemented supervisory control allocation method.

Chapter 6 Experimental Study

- Test run of the supervisory control allocation in the basin at the MCLab at MarinTek at NTNU.

Chapter 7 Conclusion

Appendix

1.5 Contribution

- Adding more data to Supervisory Control Allocation, to the authors knowledge only Ruth (2008) has done it before.
- Solving the Supervisory Control Allocation in T and α compared to decoupled generalized force done in Ruth (2008).

- Adding hysteresis effect both in power and slack variables in the Supervisory Control Allocation, compared to only power in Ruth (2008).

Chapter 2

Cybership III and MClab

2.1 Cybership III

Cybership III is a 1:30 model scale of a supply vessel designed at NTNU (See Figure 2.1). Cybership III is made from granulated reinforced polyester, as can be seen from the Figure 2.1 below. The onboard computer is running at 300 Mhz and uses the real time operating system QNX 6.3.2. Labview is runned on the host pc. A wifi router is used to connect the host pc and Cybership III together, using the 802.11g standard. The main particulars of Cybership III can be found in Table 2.1. Cybership III has 4 thrusters, 2 stern pods, one bau azimuth and one bau tunnel thruster. The thrusters can be viewed in the Figure 2.2

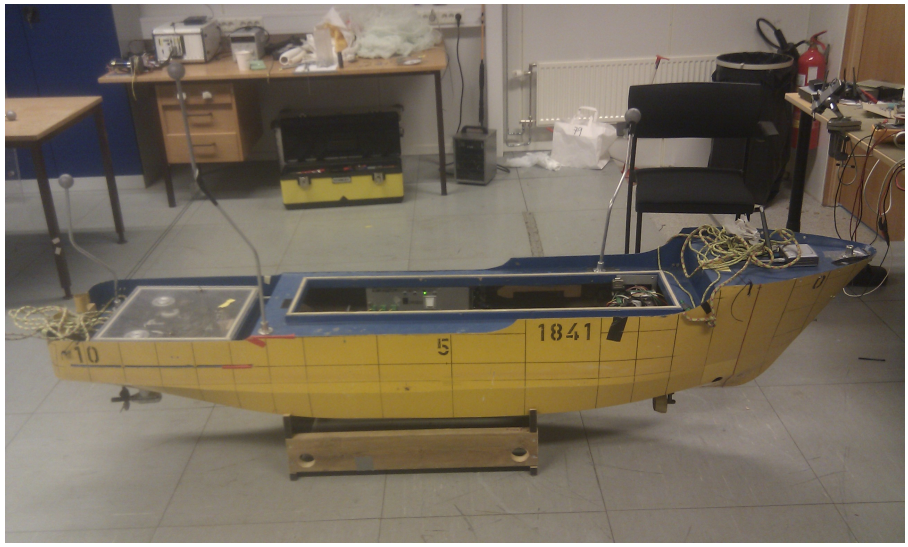

Figure 2.1: Cybership III

Hull	**Symbol**			
Model Scale	λ	30		
		Model	**Ship**	
Length between perp.	L_{pp}	1.971 m	59.13 m	
Breath	B	0.437 m	13.11 m	
Draught	T (Lpp/2)	0.153 m	4.59 m	
Weight (normal load)	M	74,2 kg	2262 tons	
Propeller data		**Pod**	**Azimuth**	**Tunnel thruster**
Max. rotational speed	n_{max}	40 rps	80 rps	80 rps
Estimated thrust				
Max Thrust (Bollard pull)	T_{max}	21.9 N	10 N	7 N
Min Thrust (Bollard pull)	T_{min}	-21.9 N	-10 N	-7 N

Table 2.1: Main particulars of Cybership III

(a) Stern Starboard and Port pods (b) Bau Azimuth

Figure 2.2: Cybership III thrusters

However the tunnel thruster is not working as it currently only has two states, zero thrust or full thrust respectively. The tunnel thruster will not be used in this paper. The position of the different thrusters are in Table 2.2 below

Thruster	$x[m]$	$y[m]$
Stern Starboard Pod	-0.875	0.123
Stern Port Pod	-0.875	-0.123
Bau Azimuth	0.55	0.0

Table 2.2: Thruster positions for CS3

Four markers is mounted on Cybership III for position detection. 3 cameras are mounted on a rail at the end of the basin at the Marine Cybernetics Lab (See Section 2.2.1). The positioning systems gives real time data of the position of the Cybership III in real-time and are transported to the Wifi-router using UDP-protocol. Position is given in 6-DOF.

2.2 Marine Cybernetics Lab

The Marine Cybernetics Laboratory (MClab) is an experimental laboratory located at MARINTEK in Trondheim. MClab is used for

testing of marine control system on ships, rigs and underwater vehicles, MCLab (2012).

2.2.1 Capacities

Basin

Tank Dimensions are

Length	$40\ [m]$
Breadth	$6.45\ [m]$
Depth	$1.5\ [m]$

Table 2.3: Basin main dimension in MCLab

A ramp and a sink is located at the end of basin to damp out waves created by the wave maker to reduce interference. The basin can be viewed in Figure 2.3 below.

Figure 2.3: MCLab basin

Wave maker

The wave maker is a 6 meter width single paddle and operates with a electric servo actuator. The wave maker is equipped with a Active Wave Absorption Control System (AWACKS 2). DHI Wave Synthesizer is installed and can produce regular and irregular waves. A designated control computer is used to produce the waves. The wave maker can be seen in Figure 2.4.

Capacity of the wave maker

- Available spectra: JONSWAP, Pierson-Moskowitz (PM), Bretschneider, ISSC, ITTC
- Regular waves Hs < 0.25 m, T = 0.3 - 3 s
- Irregular waves Hs < 0.15 m, T = 0.6 - 1.5 s
- Wave controller update rate = 10 Hz
- Speed limit = 1.2 m/s

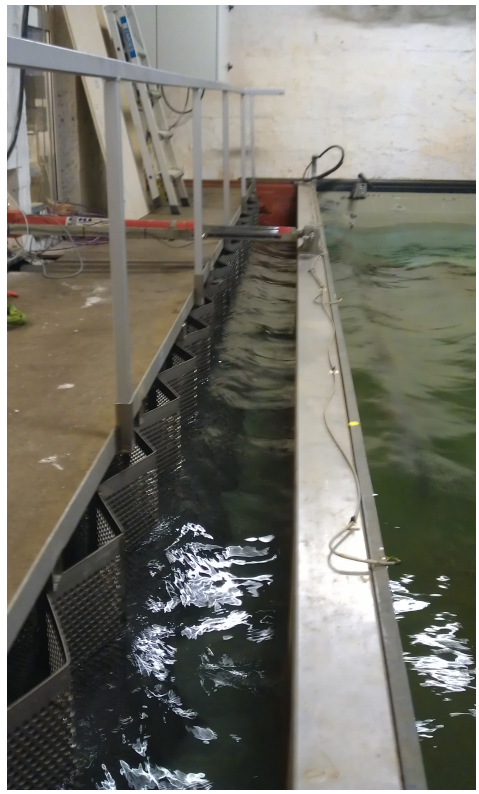

Figure 2.4: Wave maker in the MCLab basin

Real-Time Positioning system

The real-time positioning system is delivered by Qualisys (Qualisys (2012)) and consists of 3 Qqus cameras and the Qualisys Track Manager (QTM). The Qqus cameras are mounted on a moveable carriage, which can be moved to either ends of the basin. The carriage can be viewed at the end of the basin in Figure 2.3. One of the Qqus cameras can be seen in Figure 2.5.

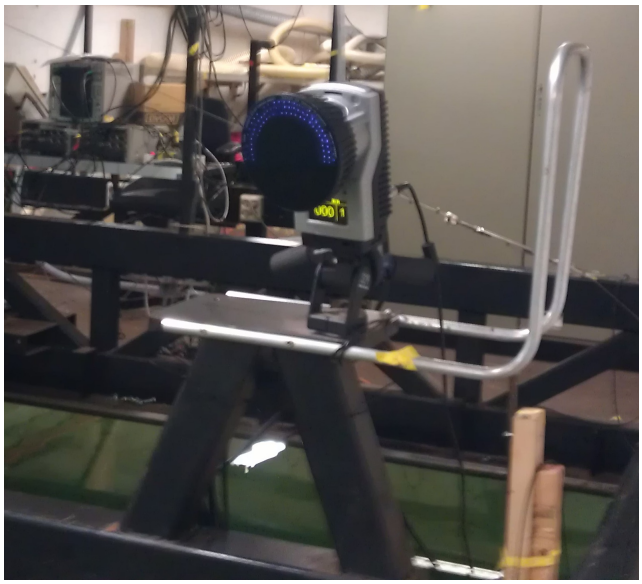

Figure 2.5: Qqus camera in MCLab mounted on carriage

A designated computer with the QTM software calculates the position of Cybership III and transmit the coordinates wireless to Cybership III (UDP protocol).

2.2.2 RT-Lab

RT-lab from Opal-RT Technologies (OpalRT (2012)) provides real-time simulation tools. RT-lab is fully integrated with Matlab/Simulink. RT-lab is used onboard Cybership III and on the host computer. RT-lab comes with an easy interface to connect Simulink models to be compiled for a designated target (In this case Cybership III). The RT-lab interface provides signals for starting/stopping execution, monitor and send signals to Cybership III. Signals between the host pc and Cybership III is synchronized to ensure a real-time system.

Chapter 3

Cybership III Modelling

Cybership III comes with a extensive modelling part, both the vessel itself and the different thrusters. However in model-scale the thruster modelling does not apply as there are no real data to calculate the thruster losses, and no proper scaling is provided for these types for modelling. This section will contain the modelling part for Cybership III with the theory behind it.

3.1 Vessel Kinematics and Kinetics

In this paper the vectorial representation for marine crafts from Fossen (2011) has been used. The parameters of this model is well known in the maritime community and is not discussed here in great detail. For more information regarding these models, degrees of freedom and reference frames please see Appendix A.2.

An extensive simulation verification was done in Børhaug (2012) on CyberShip III. New data such as current and wind coefficients for CyberShip III was found compared to simulation implementations done previous years. These new parameters will be used in this thesis.

The vessel kinematics and kinetics for low frequency motion can be

written as follows respectively

$$\dot{\boldsymbol{\eta}} = \mathbf{J}(\boldsymbol{\eta})\boldsymbol{\nu} \tag{3.1}$$

$$\boldsymbol{M}\dot{\boldsymbol{\nu}} + \boldsymbol{C}_{RB}(\boldsymbol{\nu})\boldsymbol{\nu} + \boldsymbol{C}_A(\boldsymbol{\nu}_r)\boldsymbol{\nu}_r + \boldsymbol{D}_L(\boldsymbol{\nu}_r)\boldsymbol{\nu}_r + \mathbf{G}(\boldsymbol{\eta}) = \boldsymbol{\tau}_{thr} + \boldsymbol{\tau}_{env} \tag{3.2}$$

where the 6 degrees of freedom is

$$\boldsymbol{\eta} = [x,\ y,\ z,\ \phi,\ \theta,\ \psi]^T \tag{3.3}$$

$$\boldsymbol{\nu} = [u,\ v,\ w,\ p,\ q,\ r]^T \tag{3.4}$$

by the SNAME (1950)-convention. $\mathbf{J}(\boldsymbol{\eta})$ includes the roation matrix from body-frame to the earth-fixed frame and the transformation matrix. $\mathbf{M}$ denotes the inertia matrix including both the rigid body mass and added mass matrices. $\mathbf{C}_{RB}$ and $\mathbf{C}_A$ is the Coriolis and centripetal matrices for rigid body and added mass respectively. $\mathbf{D}_L$ and $\mathbf{G}(\boldsymbol{\eta})$ is the linear damping matrix and restoring force matrix respectively.

3.2 Environmental Loads

3.2.1 Wave Loads

Wave loads are calculated based on the incoming waves, a realization such as JONSWAP (Hasselman et al., 1973) wave spectrum defines the realization of the waves. The JONSWAP wave spectrum is based upon collected data from the North Sea. The North Sea is a area where a lot of oil and gas activities are happening and therefore DP operation which makes the wave spectrum suitable for DP simulation studies. An example of the wave spectrum can be viewed in the Figure 3.1. The wave spectrum $S(\omega, \psi)$ (as seen in Figure 3.1) is acoording to Myrhaug (1993) composed of a frequency spectrum and a spreading function as follows $S(\omega, \psi) = S(\omega)f(\psi - \psi_0)$, where $S(\omega)$ is the frequency function and $f(\psi - \psi_0)$ is the spreading function respectively. The spreading function is designed in such a way that $f(\psi_0)$ is the most dominating direction. Total wave power can be calculated by the following equation

$$\int_0^\infty \int_{\psi_0-\pi}^{\psi_0+\pi} S(\omega, \psi) d\psi d\omega \tag{3.5}$$

According to Myrhaug (1993) the most commonly used spreading function is formulated as follows

$$f(\psi - \psi_0) = \begin{cases} \dfrac{2^{2s-1}s!(s-1)!}{\pi(2s-1)!}, & \text{for } -\dfrac{\pi}{2} < (\psi - \psi_0) < \dfrac{\pi}{2} \\ 0, & \text{elsewhere} \end{cases}, \tag{3.6}$$

where s is an integer. Recommended value for JONSWAP is $s = 2$. Higher values of s centers the wave energy around the mean direction ψ_0.

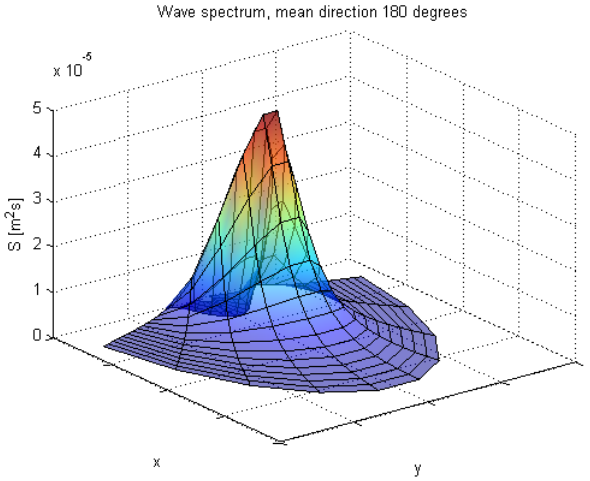

Figure 3.1: JONSWAP wave spectrum, Hs = 0.04m

The relationship between the wave amplitude (ζ_a) and the wave spectrum ($S(\psi)$) can be found by

$$\zeta_{aqr} = \sqrt{2S(\omega_q, \psi_r)\Delta\omega\Delta\psi} \tag{3.7}$$

where q and r defines the rectangle used in the Riemann integral of (3.5). And $\Delta\omega$ and $\Delta\psi$ denotes the difference between successive frequencies and spreading parameter respectively. We can then define total surface elevation for the position (x, y) at time t with N frequencies and M

directions according to Faltinsen (1993) as follows

$$\zeta(x,y,t) = \sum_{q=1}^{N}\sum_{r=1}^{M}\sqrt{2S(\omega_q,\psi_r)\Delta\omega\Delta\psi}\cdot \sin(\omega_q t + \phi_{qr} - k_q(x\cos\psi_r + y\sin(\psi_r + \epsilon_{qr})) \quad (3.8)$$

where ϕ_{qr} is the phase angle, k_q the wave number and ϵ_{qr} is a random phase angle. The wave number can be found for deep water by the dispersion relation $\omega_q^2 = kg$, where g is the Earth's acceleration of gravity. The wave number can also be found by $k = 2\pi/\lambda_q$ where λ_q is the wave length. The realization of the JONSWAP spectrum in Figure 3.1 can be viewed in Figure 3.2 below.

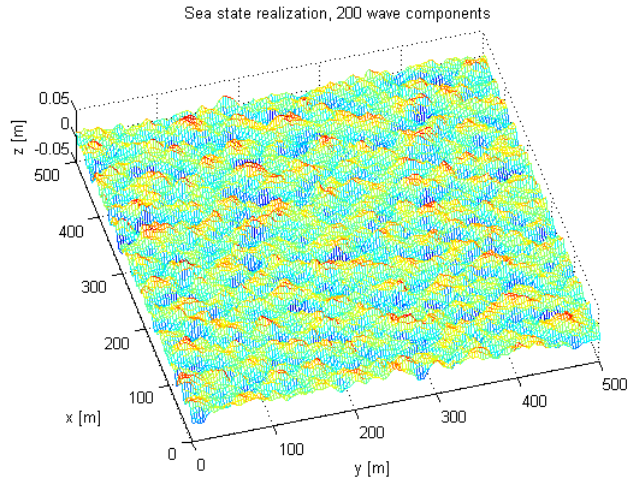

Figure 3.2: Realization of JONSWAP wave spectrum, Hs = 0.04m

Vessels loads can be divided into two different components, one low frequency (LF) model and one wave frequency (WF) model respectively. The low frequency model is driven by mean and slowly varying wave loads, current, wind loads and thruster forces. Wave Frequency is driven by 1st order wave loads. In this thesis only the LF wave loads model is used. A general equation for slowly varying wave loads can from

Faltinsen (1993) formally be written as

$$\begin{aligned}\boldsymbol{\tau}_i^{SV} = &\sum_{j=1}^{N}\sum_{k=1}^{N} A_j A_k [T_{jk}^{ic} cos\{(\omega_k - \omega_j)t + (\epsilon_k - \epsilon_j)\} \\ &+ T_{jk}^{is} sin\{(\omega_k - \omega_j)t + (\epsilon_k - \epsilon_j)\}] \end{aligned} \tag{3.9}$$

where A_i is the wave amplitudes, ω_i the wave frequencies and ϵ_i a random phase angles. While the coefficients T_{jk}^{ic} and T_{jk}^{is} can be interpreted as second-order transfer functions. However, (3.9) can be quite time consuming as the number of wave components to look over is N^2. A simplification can be done according to Faltinsen (1993) by finding the mean value of (3.9). The mean value of the oscillating terms of (3.9) is viewed to be zero over a long time period and the only time independent term remaining is the case when $k = j$. Resulting equation, Faltinsen (1993), becomes thus

$$\overline{\boldsymbol{\tau}_i^{SV}} = \sum_{j=1}^{N} A_j^2 T_{jj}^{ic} \tag{3.10}$$

where then $A_j^2 T_{jj}^{ic}$ is the mean wave load in direction i. In this thesis, the transfer function T_{jj}^{ic} is pre calculated for different frequencies and degrees of freedom, and interpolation is used between the wave frequencies and non-pre-calculated in T_{jj}^{ic}.

3.2.2 Wind Loads

Wind loads can be divided into two parts, one mean and slowly varying and one oscillating part also known as gust, Sørensen (2011). The mean wind velocity at a certain elevation z can be expressed according to Myrhaug (1993) as follows

$$\frac{\bar{U}(z)}{\bar{U}_{10}} = \frac{5}{2}\sqrt{\kappa}\ln\frac{z}{z_0};\;\; z_0 = 10\exp(-\frac{2}{5\sqrt{\kappa}}) \tag{3.11}$$

where $\bar{U}_{10}$ is the mean wind speed at 10 meter elevation during 1 hour, and κ is the sea surface drag coefficient. In this paper only the mean

wind velocity $\bar{U}$ part will be used, slowly-varying wind amplitude will be omitted. Mean wind velocity will be used in the realization of the gust and will be explained later. The slowly-varying wind direction can be implemented as a Gauss-Markov Process (Fossen (2002))

$$\psi = \bar{\psi} + \psi^V \tag{3.12a}$$

$$\dot{\psi}^V = w - \mu\psi^V \tag{3.12b}$$

$$\psi^V_{min} \leq \psi^V \leq \psi^V_{max} \tag{3.12c}$$

where the wind direction ψ is described by a mean value $\bar{\psi}$ and a Gauss-Markov varying part ψ^V. w is Gaussian white noise and $\mu \geq 0$ a positive constant. In case $\mu = 0$ (3.12b) is called a random walk process. The varying part is also limited by a upper and lower bound, ψ^V_{max} and ψ^V_{min} respectively.

Wind gust is commonly described by a wind spectrum. The two most common wind spectra is the Harrison and NORSOK wind spectra Sørensen (2011). Harrison wind spectrum is based upon measurement taken over land, while the NORSOK wind spectrum is based upon measurement in the North Sea and thus be used in this paper. The NORSOK wind spectrum can be written as follows

$$S(f) = 320\frac{(\frac{\bar{U}_{10}}{10})^2(\frac{z}{10})^{0.45}}{(1+x^n)^{\frac{5}{3n}}}, \quad n = 0.468 \tag{3.13a}$$

$$x = 172f \cdot (\frac{z}{10})^{\frac{2}{3}}(\frac{\bar{U}_{10}}{10})^{\frac{-3}{4}} \tag{3.13b}$$

where z is the elevation in meters, f frequency in Hz. The spectrum can be viwed in Figure 3.3 below.

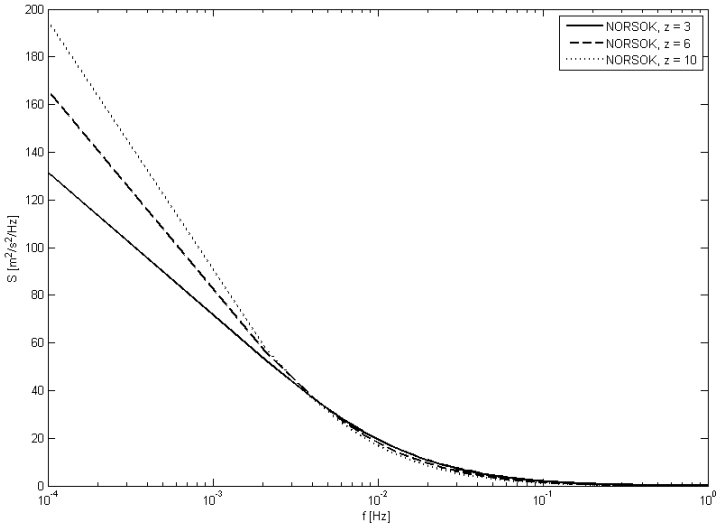

Figure 3.3: NORSOK spectrum with $\bar{U}_{10} = 10m/s$

Realization of the wind state is done by superposing the gust realization and the mean wind at the desired elevation (Sørensen (2011)). The realization of the gust is done similar to the waves. Since the wind spectrum has only the frequency as a parameter the relationship between the spectrum and the amplitude of the gust can be expressed as follows

$$A_{i,wind} = \sqrt{2S(f_i)\Delta f_i} \tag{3.14}$$

Total wind realization can then be expressed as follows

$$U(z,t) = \bar{U}(z) + \sum_{i=1}^{N} \sqrt{2S(f_i)\Delta f_i} cos(2\pi f_i t + \epsilon_i) \tag{3.15}$$

where ϵ_i is evenly distributed randomized phase angle. Wind loads can

then be calculated by typical drag functions as stated in Fossen (2011)

$$\boldsymbol{\tau}_{wind} = \frac{1}{2}\rho_a V_{rw}^2 \begin{bmatrix} C_{wx}(\gamma_{rw})A_{Fw} \\ C_{wy}(\gamma_{rw})A_{Lw} \\ C_{wz}(\gamma_{rw})A_{Fw} \\ C_{wk}(\gamma_{rw})A_{Lw}H_{Lw} \\ C_{wm}(\gamma_{rw})A_{Fw}H_{Fw} \\ C_{wn}(\gamma_{rw})A_{Lw}L_{oa} \end{bmatrix} \tag{3.16a}$$

$$V_{rw} = \sqrt{u_{rw}^2 + v_{rw}^2} \tag{3.16b}$$

$$\gamma_{rw} = -\text{atan2}(v_{rw}, u_{rw}) \tag{3.16c}$$

where ρ_a is the air density, γ_{rw} and V_{rw} is the relative wind direction and speed respectively. The decomposed relative wind speed u_{rw} and v_{rw} is found by the total wind realization (3.15), the wind direction (3.12) and vessel direction. $C_{wx}, C_{wy}, C_{wz}, C_{wk}, C_{wm}C_{wn}$ are the wind coefficients, while A_{Lw} and A_{Fw} are the lateral and frontal projected surface surface area of the vessel respectively. H_{Lw} and H_{Fw} are the centroids above the water line of the lateral and frontal projected areas (Fossen, 2011). L_{oa} is the vessel's length over all.

3.2.3 Current Loads

In this thesis, the current is simulated as a 2-D phenomenon in x and y direction in the NED-reference frame. The current model is quite similar to the wind force calculation in (3.16a) and based on the current model proposed in IMCA's Specification for DP capability plots (IMCA (2000)). IMCA only includes 3-DOF model, but similar to the wind force the centroids under the water line is added to get 6-DOF.

$$\boldsymbol{\tau}_{curr} = \frac{1}{2}\rho_w V_{rc}^2 \begin{bmatrix} C_{cx}(\gamma_{rc})BT \\ C_{cy}(\gamma_{rc})TL_{pp} \\ 0 \\ C_{ck}(\gamma_{rc})TL_{pp}H_{Lc} \\ C_{cm}(\gamma_{rc})BTH_{Fc} \\ C_{cn}(\gamma_{rc})TL_{pp}^2 \end{bmatrix} \tag{3.17}$$

where ρ_w is the water density. B, T and L_{pp} is the breadth, draft and length between perpendicular respectively. H_{Lc} and H_{Fc} are the same as H_{Lw} and H_{Fw} just under the water line. The rest of the parameters are similar to the wind model, and thus not discussed further here.

3.3 Total Environmental Load

The total environmental loading is then combination of the wind, current, and wave loadings

$$\boldsymbol{\tau}_{env} = \boldsymbol{\tau}_{wind} + \boldsymbol{\tau}_{curr} + \overline{\boldsymbol{\tau}_i^{SV}} \tag{3.18}$$

3.4 DP Controller

In this thesis, a simple 3-DOF nonlinear PID-controller is used, Fossen (2011)

$$\boldsymbol{\tau}_c = \boldsymbol{\tau}_{pid} := \mathbf{R}(\psi)^T(-\mathbf{K}_p\tilde{\boldsymbol{\eta}} - \mathbf{K}_d\dot{\tilde{\boldsymbol{\eta}}} - \mathbf{K}_i\int_0^t \tilde{\boldsymbol{\eta}}\ \delta t) \tag{3.19}$$

where $\tilde{\boldsymbol{\eta}} = \boldsymbol{\eta} - \boldsymbol{\eta}_d$. And $\mathbf{K}_p$, $\mathbf{K}_i$ and $\mathbf{K}_d$ is the proportional, integrative and derivative controller matrices respectively. This is a well known controller, and will not be discussed further here. (Please see Fossen (2011) and Sørensen (2011) for more information.)

3.5 Observer

For the nonlinear passive observer the following prerequisites are needed and assumed as stated in Fossen (2011)

1. Assume that the rotation matrix can be written as $\mathbf{R}(\psi) = \mathbf{R}(y_3)$, which implies $\psi \approx \psi + \psi_w = y_3$.

This will be a fair estimation in normal conditions as the wave induced heading noise ψ_w will be less than 5 degrees in extreme weather conditions, and less than 1 degree in normal conditions (Please see Fossen (2011) for more information)

2. The vessel mass matrix is assumed to be static, i.e $\dot{\mathbf{M}} = \mathbf{0}$.

3.5.1 Nonlinear Passive Observer Equations

The observer is in 3-DOF

$$\dot{\hat{\boldsymbol{\xi}}} = \mathbf{A}_w\hat{\boldsymbol{\xi}} + \mathbf{K}_1(\boldsymbol{\omega}_0)\tilde{\mathbf{y}} \tag{3.20a}$$

$$\dot{\hat{\boldsymbol{\eta}}} = \boldsymbol{R}(y_3)\hat{\boldsymbol{\nu}} + \mathbf{K}_2\tilde{\mathbf{y}} \tag{3.20b}$$

$$\dot{\hat{\mathbf{b}}} = -\mathbf{T}^{-1}\hat{\mathbf{b}} + \mathbf{K}_3\tilde{\mathbf{y}} \tag{3.20c}$$

$$\mathbf{M}\dot{\hat{\boldsymbol{\nu}}} = -\mathbf{D}\hat{\boldsymbol{\nu}} + \mathbf{R}^T(y_3)\hat{\boldsymbol{b}} + \boldsymbol{\tau} + \mathbf{R}^T(y_3)\mathbf{K}_4\tilde{\mathbf{y}} \tag{3.20d}$$

$$\hat{\mathbf{y}} = \hat{\boldsymbol{\eta}} + \mathbf{C}_w\hat{\boldsymbol{\xi}} \tag{3.20e}$$

where $\tilde{\mathbf{y}} = \mathbf{y} - \hat{\mathbf{y}}$ is the estimation error and the matrices $\mathbf{K}_1(\boldsymbol{\omega}_0)$, $\mathbf{K}_2$, $\mathbf{K}_3$ and $\mathbf{K}_4$ are the observer gains. The observer gains has the following structure

$$\mathbf{K}_1(\boldsymbol{\omega}_o) = \begin{bmatrix} \text{diag}\{K_{11}(\omega_{o1}),\ K_{12}(\omega_{o2}),\ K_{13}(\omega_{o3})\} \\ \text{diag}\{K_{14}(\omega_{o1}),\ K_{15}(\omega_{o2}),\ K_{16}(\omega_{o3})\} \end{bmatrix} \tag{3.21a}$$

$$\mathbf{K}_2 = \text{diag}\{K_{21},\ K_{22},\ K_{23}\} \tag{3.21b}$$

$$\mathbf{K}_3 = \text{diag}\{K_{31},\ K_{42},\ K_{43}\} \tag{3.21c}$$

$$\mathbf{K}_4 = \text{diag}\{K_{41},\ K_{42},\ K_{43}\} \tag{3.21d}$$

As can be seen from (3.21a) $\mathbf{K}_1(\boldsymbol{\omega}_o)$ is a function of the wave spectra peak frequencies in surge, sway and yaw ($\boldsymbol{\omega}_o = [\omega_{o1}, \omega_{o2}, \omega_{o3}]$). Surge, sway and yaw is decouple in the observer.

In order for the estimator to be passive the observer has to satisfy the Kalman-Yakubovich-Popov (KYP) lemma, Fossen (2011). This is done by the following equations

$$K_{1i}(\omega_{oi}) = -2(\zeta_{ni} - \lambda_i)\frac{\omega_{ci}}{\omega_{oi}} \tag{3.22a}$$

$$K_{1(i+3)}(\omega_{oi}) = 2\omega_{oi}(\zeta_{ni} - \lambda_i) \tag{3.22b}$$

$$K_{2i} = \omega_{ci} \tag{3.22c}$$

$$\frac{1}{T_i} \ll \frac{K_{3i}}{K_{4i}} < \omega_{oi} < \omega_{ci} \tag{3.22d}$$

$$(i = 1, \cdots, 3)$$

where λ_i is the relative damping ratio of the wave spectrum. $\zeta_i > \lambda_i$ determines the notch effect of the observer. ω_{oi} is the wave spectrum peak frequency and $\omega_{ci} > \omega_{oi}$ is the filter cutoff frequency. The effect from these parameters can be seen in frequency response of the nonlinear passive observer in Figure 3.4

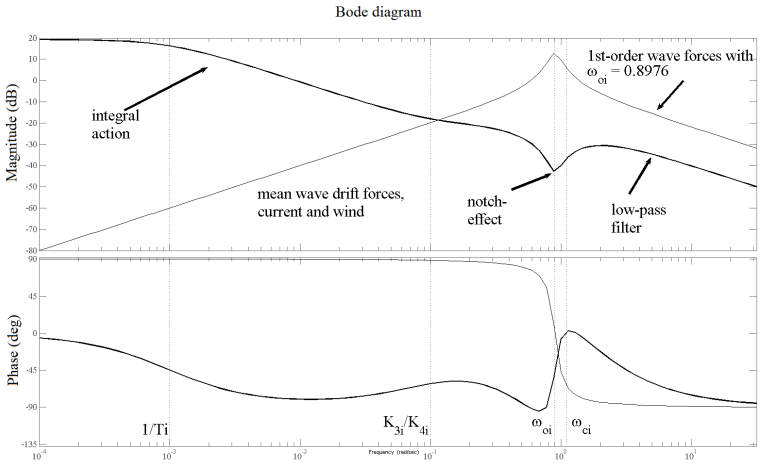

Figure 3.4: Bode plot showing the response of the Nonlinear Passive Observer. Generated using ExPassiveObs.m in the MSSToolbox (2012)

3.6 Control Allocation

The control allocation will be discussed in more details in Chapter 4

3.7 Propulsion Units

3.7.1 Modelling and low-level controller

The shaft speed reference goes through a low-pass-filter, simulating a well tuned shaft speed PID-controller. The propeller thrust is then calculated by 1-quadrant model (A.5), restated there for convenience

$$T_p = \text{sign}(n)\rho K_T(J_a)n^2D^4 \tag{3.23}$$

$K_T(J_a)$ is often in the literature simplified as a linear approximation of Figure A.1. Here a quadratic linear approach is given to approximate the curvature of Figure A.1 a little better than a pure linear approximation. The approximation used is

$$K_T(J_a) = a_2J_a^2 + a_1J_a + a0 \tag{3.24}$$

where the approximation parameters for Cybership III is as follows

Thruster	a_2	a_1	a_0
Bau Azimuth	-0.1389	-0.4250	0.6016
Stern Pods	-0.0475	-0.1452	0.2056

Table 3.1: K_T approximation parameters

The approximation of the propeller characteristics can be viewed in Figure 3.5 below

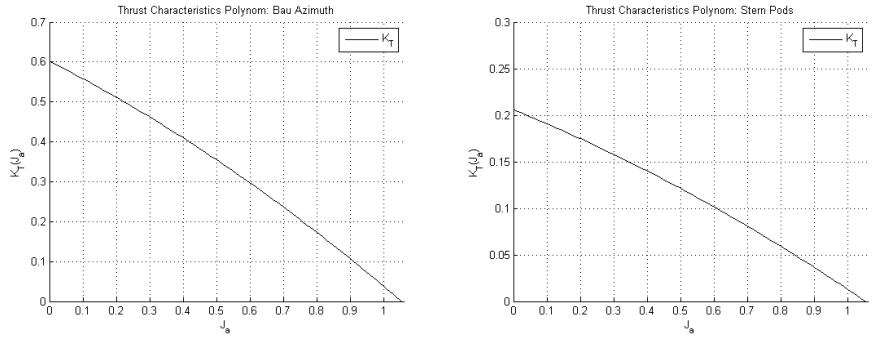

(a) Bau Azimuth thrust characteristics $K_T(J_a)$

(b) Stern Starboard and Port pods thrust characteristics $K_T(J_a)$

Figure 3.5: Thrust characteristics for Cybership III described by a polynom in (3.24). Where the thrust characteristic $K_T(J_a)$ is described by the advance velocity J_a

The advance velocity J_a is found by (A.8) restated here for convenience

$$J_a := \frac{V_A}{nD} \tag{3.25}$$

where then the inflow velocity is modelled as a simple function defined in Carlton (1994)

$$V_a = U_r(1 - w_f) \tag{3.26}$$

where $U_r = \sqrt{u_r^2 + v_r^2}$ and w_f is the wake fraction, typically in the range of $0 < w_f < 0.4$. In this paper $w_f = 0.2$.

The total system will be simulated using "Open-water propeller characteristics" and "Propeller shaft dynamics" blocks in the MSSToolbox (2012). The "Open-water propeller characteristics" is a 2-quadrant where the 2nd quadrant is found by scaling the parameters from the 1st quadrant model by a scalar. In this paper the 2nd quadrant parameters will be scaled down 20% of the 1st quadrant parameters.

Inverse Thrust Reference

Typically the shaft speed reference is a reverse mapping of (3.23), (Sørensen, 2011), as follows

$$n_{ref} = \text{sign}(T_{ref})\sqrt{\frac{|T_{ref}|}{\rho D^4 K_{TC}}} \tag{3.27}$$

where K_{TC} is $K_T(J_a = 0)$. Due to the lack of data for reverse thrust characteristics K_{Tr} in this thesis, a different reverse mapping will be used. The reverse mapping from thrust to shaft speed in RPM implemented in the original code of Cybership III is

$$n^{pos}_{ref,RPM} = \sqrt{|T_{ref}|}K_{f,RPM} \tag{3.28a}$$

$$n^{neg}_{ref,RPM} = -\sqrt{|T_{ref}|}K_{b,RPM} \tag{3.28b}$$

where $n^{pos}_{ref,RPM}$ and $n^{neg}_{ref,RPM}$ is the positive and negative shaft speed reference in RPM respectively. And $K_{f,RPM}$ and $K_{b,RPM}$ is the forwards and backwards mapping parameters. The mapping data used is as follows

Thruster	$K_{f,RPM}$	$K_{b,RPM}$
Bau Azimuth	$4.6127 \cdot 10^3$	$4.7673 \cdot 10^3$
Stern Pods	$0.3933 \cdot 10^3$	$0.4724 \cdot 10^3$

Table 3.2: Cybership III: Thrust to shaft speed in RPM mapping parameters

Compared to direct reverse mapping of (3.27) with the data from Table 3.1 the mapping in (3.28) using the paramters in Table 3.2 will give slighly larger shaft speed. However the data from Table 3.2 will give larger shaft speed to prevent mismatch between the actual thrust and thrust reference due to thrust deduction descriped in Sørensen (2011).

Due to lack of torque characteristics for the propellers, the power for each thruster was found by reading the power output on each thruster at 1200

RPM in power measurements done by Ruth (2008). And then combine (3.28) and (A.7) to find the thrust to power relationship:

$$P = K_{pt}|T|^{3/2} \tag{3.29}$$

with the following parameters for the Cyberhship III thrusters

Thruster	K_{pt}
Bau Azimuth	41.9190
Stern Pods	1.5844

Table 3.3: Cybership III: thrust to power relationship parameters

Chapter 4

Control Allocation

4.1 Introduction

In this paper a control allocation method using convex linearly constrained quadratic optimization problem will be used. The constraints are based upon the commanded generalized force, mechanical constraints in both maximum azimuth angles and thrust production. Rate constraints due to mechanical constraints assosiated with the thrusters will be used. The solution will be found by using Quadratic Programming (QP). The benefits of using QP methods are that it is guaranteed that the existence of only one minimum or a infeasibility solution will be found, Nocedal and Wright (2006). In the case of convex optimization region it is guaranteed to find this minimum solution. If the QP-problem does not contain any rate constraints, with a global optimization region, the global minimum solution will be found. However if rate constraints are included, only local minimum solutions can be expected to be found as the optimization region is a local subset of the global region. The QP-method in this thesis will be an iterative method, where the previous solution will be used to modify the constraints and cost function.

The general thrust allocation problem used as fundament in this thesis can be formulated as (4.1) - (4.6). This general thrust allocation problem

will be changed during this thesis to take different constraints into account. The notation and formulation is taken from Ruth (2008).

$$[\mathbf{T}_d,\ \boldsymbol{\alpha}_d] = \underset{\mathbf{T}_d \subset \mathcal{S}_{\mathbf{T}},\ \boldsymbol{\alpha}_d \subset \mathcal{S}_{\boldsymbol{\alpha}}}{\operatorname{argmin}} (J(\mathbf{T},\ \boldsymbol{\alpha},\ \mathbf{s},\ \boldsymbol{\tau}_c)), \tag{4.1}$$

subject to

$$\mathbf{B}(\boldsymbol{\alpha}_d)\mathbf{T}_d + \mathbf{s} = \boldsymbol{\tau}_c \tag{4.2}$$
$$\mathbf{T}_{min} \leq \mathbf{T} \leq \mathbf{T}_{max} \tag{4.3}$$
$$\boldsymbol{\alpha}_{min} \leq \boldsymbol{\alpha} \leq \boldsymbol{\alpha}_{max} \tag{4.4}$$
$$\boldsymbol{\Delta}\mathbf{T}_{min} \leq \boldsymbol{\Delta}\mathbf{T} \leq \boldsymbol{\Delta}\mathbf{T}_{max} \tag{4.5}$$
$$\boldsymbol{\Delta}\boldsymbol{\alpha}_{min} \leq \boldsymbol{\Delta}\boldsymbol{\alpha} \leq \boldsymbol{\Delta}\boldsymbol{\alpha}_{max} \tag{4.6}$$

where J in (4.1) is the cost function. The cost function can contain minimization of power, singularity avoidance, maximization of maneuverability or other design choices. $\mathbf{T}_d \in \mathbb{R}^{n_t}$ is the desired thrust force with values from the admissible thrust set $\mathcal{S}_{\mathbf{T}} \in \mathbb{R}^{n_t}$. $\boldsymbol{\alpha}_d \in \mathbb{R}^{n_t}$ is the desired thrust direction with values from the admissible directions set $\mathcal{S}_{\boldsymbol{\alpha}} \in \mathbb{R}^{n_t}$. $\mathbf{s} \in \mathbb{R}^m$ is the slack variable that ensures that there always exists a solution to the equality constraint (4.2). $\mathbf{s}$ is typically weighted high in the cost function J compare to $\mathbf{T}$ and $\boldsymbol{\alpha}$. This is to not let $\mathbf{s}$ interfere the goal of the thruster allocation problem to keep $\mathbf{B}(\boldsymbol{\alpha}_d)\mathbf{T}_d - \boldsymbol{\tau}_c$ as small as possible. $n_t \in \mathbb{R}$ is the number of thrusters, and $m \in \mathbb{R}$ is the number of controlled degrees of freedom. $\mathbf{B} \in \mathbb{R}^{m \times n_t}$ is the thruster configuration matrix determined by the location and direction of each individual thruster, as explained (as $\mathbf{T}(\boldsymbol{\alpha})$) in Fossen (2011). The 3-DOF configuration matrix is as follows from Fossen (2011)

$$\mathbf{B}(\boldsymbol{\alpha}) = \begin{bmatrix} cos(\alpha_1) & \cdots & cos(\alpha_{n_t}) \\ sin(\alpha_1) & \cdots & sin(\alpha_{n_t}) \\ l_{x_1} sin(\alpha_1) - l_{y_1} cos(\alpha_1) & \cdots & l_{x_{n_t}} sin(\alpha_{n_t}) - l_{y_{n_t}} cos(\alpha_{n_t}) \end{bmatrix} \tag{4.7}$$

where α_i can be fixed or rotatable. l_{x_i} and l_{y_i} are the moment arms for the specific thruster.

A simplification done in this thesis is to let the rotating stern pods to only produce positive thrust. This is because often in mechanical design choices the thrusters should mainly be used in one direction only. It might also be undesired to let the propeller shaft to go both ways as rapid

changes from positive and negative shaft speed can cause high strain on the mechanical system. Even though the thruster has the possibility to produce both positive and negative thrust, the thrusters normally is designed to be more efficient in one direction. This comes from how the pitch on the propeller blades are designed.

4.2 Allocation Problem structure

Proposed control allocation problem in this thesis is mainly focused on power-efficiency, and will be solved by using quadratic programming (QP). The algorithm will be optimized based upon Δ_α and Δ_T as a singularity avoidance strategy from Johansen et al. (2004) will be used.

4.2.1 Cost Function Structure

Propeller power consumption is in the term of $|T|^{\frac{3}{2}}$ as can be seen by combining (A.5) and (A.7) to

$$P = \frac{2\pi K_{QC}}{\sqrt{\rho} D K_{TC}^{3/2}} |T|^{3/2} \tag{4.8}$$

where K_{QC} and K_{TC} is $K_Q(J_a = 0)$ and $K_T(J_a = 0)$ respectively. However, since a QP optimization algorithm has been used, it is not possible to use (4.8) directly as it is not quadratic. In Ruth (2008) a different approach was proposed:

$$J_T = \left|\left| \frac{\mathbf{W}_u}{\sqrt[4]{|\mathbf{T}_{d,prev}|}} \mathbf{T}_d \right|\right|_2^2 \tag{4.9}$$

where the thrust from the previous step is included to modify the cost function is such a way that the cost approaches $|T_d|^{3/2}$. This can be seen

from Ruth (2008) by the following limit

$$\begin{aligned}\lim_{T_d \to T_{d,prev}} P_{cost} &= \lim_{T_d \to T_{d,prev}} \frac{T_d^2}{\sqrt{|T_{d,prev}|}} \\ &= |T_d|^{3/2}\end{aligned} \tag{4.10}$$

The cost function structure for thruster j was proposed by Ruth (2008) as

$$\begin{aligned}J_j^T &= q\frac{2\pi K_{QC,j}}{\sqrt{\rho}DK_{TC,j}^{3/2}}\frac{1}{\sqrt{T_{d,prev,j}}}T_{d,j}^2 \\ &= W_{u,j,j}^2\frac{1}{\sqrt{T_{d,prev,j}}}T_{d,j}^2\end{aligned} \tag{4.11}$$

where the constant q is equal to all the thrusters. q is included to get a consistent relationship between the power cost in (4.9) and the cost of not producing the correct thrust $||\mathbf{W}_s\mathbf{s}||$, Ruth (2008), and is proposed as follows

$$\frac{1}{q} = \frac{1}{n}\sum_{j=1}^{n}\left[\frac{2\pi K_{QC,j}}{\sqrt{\rho}DK_{TC,j}^{3/2}}\right] \tag{4.12}$$

q will also insure that the different thrusters are scaled compared to each other. Due to the lack of torque characteristics for Cybership III, q is found by (3.29).

In this thesis, the optimization is based upon ΔT_j instead of T_j, (4.11) must be rewritten. Using $T_j = T_{prev,j} + \Delta T_j$ we can rewrite (4.11) as follows

$$\begin{aligned}J_j^T &= W_{u,j,j}^2\frac{1}{\sqrt{T_{d,prev,j}}}T_{d,j}^2 \\ &= W_{u,j,j}^2\frac{1}{\sqrt{T_{d,prev,j}}}(T_{d,prev,j}^2 + T_{d,prev,j}\Delta T_{d,j} + \Delta T_{d,j}^2) \\ &\qquad\qquad \downarrow \\ J_j^{\Delta T} &= W_{u,j,j}^2\frac{1}{\sqrt{T_{d,prev,j}}}(\Delta T_{d,j}^2 + T_{d,prev,j}\Delta T_{d,j})\end{aligned} \tag{4.13}$$

Where we can remove $T_{d,prev,j}^2$ from the cost function as it is constant and will not change the dynamics of the quadratic solver, Nocedal and Wright (2006).

To prevent drift off due to singular cases, which might turn into using more power to regain position, a singularity avoidance is added. A simple singularity avoidance was proposed in Johansen et al. (2004). This singularity avoidance is obtained to prevent $\mathbf{B}(\boldsymbol{\alpha})\mathbf{B}(\boldsymbol{\alpha})^T$ from being singular. The cost was proposed to be

$$J_{singularity} = \frac{\rho}{\epsilon + \det(\mathbf{B})(\boldsymbol{\alpha})\mathbf{B})(\boldsymbol{\alpha})^T)} \tag{4.14}$$

where ρ is a scalar to tune either towards maneuverability or power-efficiency singularity avoidance. ϵ is a small constant to prevent the denominator in (4.14) to be zero in singular solutions. The cost is linearised similar to Johansen et al. (2004) as

$$J_{singularity}^{\boldsymbol{\Delta\alpha}} = \frac{d}{d\boldsymbol{\alpha}} \left(\frac{\rho}{\epsilon + \det(\mathbf{B})(\boldsymbol{\alpha})\mathbf{B})(\boldsymbol{\alpha})^T)} \right)_{\boldsymbol{\alpha}=\boldsymbol{\alpha}_{prev}} \boldsymbol{\Delta\alpha} \tag{4.15}$$

where the linearization in (4.15) is in this thesis found numerically based upon the maximum rate for the azimuth thrusters.

The total cost function can then be written as a sum of (4.13), (4.15) and a cost for the azimuth angles and slack variables similar to the cost function in Johansen et al. (2004)

$$\begin{aligned} J_{QP}\left(\boldsymbol{\Delta T}, \boldsymbol{\Delta\alpha}, \mathbf{s}\right) = & \sum_{i=1}^{n} \left(\frac{W_{u,j,j}^2}{\sqrt{T_{d,prev,j}} + \epsilon_T} \Delta T_{d,j}^2 + W_{u,j,j}^2 \left(\sqrt{T_{d,prev,j}} + \epsilon_T \right) \Delta T_{d,j} \right) \\ & + \boldsymbol{\Delta\alpha}^T \boldsymbol{\Omega} \boldsymbol{\Delta\alpha} + \mathbf{s}^T \mathbf{Q} \mathbf{s} \\ & + \frac{d}{d\boldsymbol{\alpha}} \left(\frac{\rho}{\epsilon + \det(\mathbf{B})(\boldsymbol{\alpha})\mathbf{B})(\boldsymbol{\alpha})^T)} \right)_{\boldsymbol{\alpha}=\boldsymbol{\alpha}_{prev}} \boldsymbol{\Delta\alpha} \end{aligned} \tag{4.16}$$

where ϵ_T is a small constant to prevent infinity cost when $T_{d,prev,j}$ is zero. And $\boldsymbol{\Omega}$ and $\mathbf{Q}$ is the weight matrices for changing azimuth angle and slack variables respectively.

4.2.2 Constraints Structure

The equality constraint in (4.2) is linearized as follows

$$\mathbf{B}(\boldsymbol{\alpha}_{prev})\boldsymbol{\Delta}\mathbf{T} + \frac{\partial}{\partial \boldsymbol{\alpha}}(\mathbf{B}(\boldsymbol{\alpha})\mathbf{T})\Big|_{\substack{\boldsymbol{\alpha}=\boldsymbol{\alpha}_{prev} \\ \mathbf{T}=\mathbf{T}_{prev}}} \cdot \boldsymbol{\Delta}\boldsymbol{\alpha} + \mathbf{s} = \boldsymbol{\tau}_c - \mathbf{B}(\boldsymbol{\alpha}_{prev})\mathbf{T}_{prev} \tag{4.17}$$

Inequality constraints (4.3) - (4.6) are as follows

$$\boldsymbol{\Delta}\mathbf{T}_- \leq \boldsymbol{\Delta}\mathbf{T} \leq \boldsymbol{\Delta}\mathbf{T}_+ \tag{4.18a}$$
$$\boldsymbol{\Delta}\boldsymbol{\alpha}_- \leq \boldsymbol{\Delta}\boldsymbol{\alpha} \leq \boldsymbol{\Delta}\boldsymbol{\alpha}_+ \tag{4.18b}$$
$$\mathbf{s}_{min} \leq \mathbf{s} \leq \mathbf{s}_{max} \tag{4.18c}$$

where $\mathbf{s}_{max}$ and $\mathbf{s}_{min}$ is large positive and negative vectors and $\boldsymbol{\Delta}\mathbf{T}_{+/-}$ and $\boldsymbol{\Delta}\boldsymbol{\alpha}_{+/-}$ are defined as the difference between the maximum allowed thrust production and maximum azimuth angle and the previous thrust and angle solution respectively. $\mathbf{T}_{+/-}$ and $\boldsymbol{\Delta}\boldsymbol{\alpha}_{+/-}$ are defined as follows

$$\boldsymbol{\Delta}\mathbf{T}_+ = \mathbf{T}_+ - \mathbf{T}_{prev} \tag{4.19a}$$
$$\boldsymbol{\Delta}\mathbf{T}_- = \mathbf{T}_- - \mathbf{T}_{prev} \tag{4.19b}$$
$$\boldsymbol{\Delta}\boldsymbol{\alpha}_+ = \boldsymbol{\alpha}_+ - \boldsymbol{\alpha}_{prev} \tag{4.19c}$$
$$\boldsymbol{\Delta}\boldsymbol{\alpha}_- = \boldsymbol{\alpha}_- - \boldsymbol{\alpha}_{prev} \tag{4.19d}$$

$\boldsymbol{\alpha}_{+/-}$ and $\mathbf{T}_{+/-}$ is defined as in Ruth (2008) as follows

$$\mathbf{T}_+ = \max\left(\min\left(\mathbf{T}_{max}, \mathbf{T}_{prev} + \dot{\mathbf{T}}_{max}\Delta t\right), \mathbf{T}_{prev} + c_1\dot{\mathbf{T}}_{min}\Delta t\right) \tag{4.20a}$$
$$\mathbf{T}_- = \min\left(\max\left(\mathbf{T}_{min}, \mathbf{T}_{prev} + \dot{\mathbf{T}}_{min}\Delta t\right), \mathbf{T}_{prev} + c_1\dot{\mathbf{T}}_{max}\Delta t\right) \tag{4.20b}$$
$$\boldsymbol{\alpha}_+ = \max\left(\min\left(\boldsymbol{\alpha}_{max}, \boldsymbol{\alpha}_{prev} + \dot{\boldsymbol{\alpha}}_{max}\Delta t\right), \boldsymbol{\alpha}_{prev} - c_1\dot{\boldsymbol{\alpha}}_{max}\Delta t\right) \tag{4.20c}$$
$$\boldsymbol{\alpha}_- = \min\left(\max\left(\boldsymbol{\alpha}_{min}, \boldsymbol{\alpha}_{prev} - \dot{\boldsymbol{\alpha}}_{max}\Delta t\right), \boldsymbol{\alpha}_{prev} + c_1\dot{\boldsymbol{\alpha}}_{max}\Delta t\right) \tag{4.20d}$$

where Δt is the sample time and $c_1 \subset [0, 1\rangle$. $\mathbf{T}_{prev} + c_1\dot{\mathbf{T}}_{min}\Delta t$ will ensure that a solution will be found even though the previous operating point is outside the maximum constraint.The same applies for $\mathbf{T}_-$, $\boldsymbol{\alpha}_+$ and $\boldsymbol{\alpha}_-$. c_1 is set to 0.9 in this thesis similar to Ruth (2008). The results of the constraints in (4.20) can be seen in Figure 4.1 below.

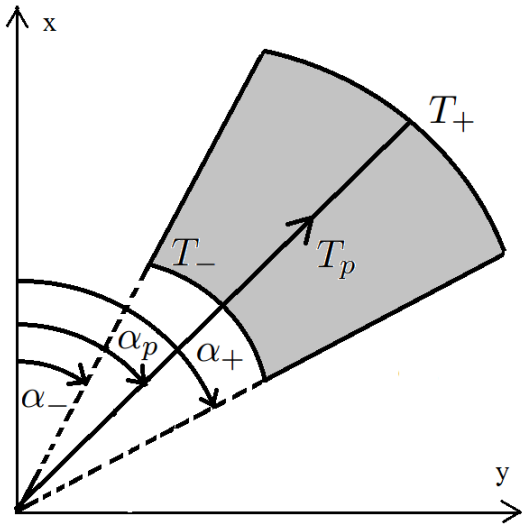

Figure 4.1: Inequality constraints resulting from (4.20)

4.2.3 QP Solver

The solver can then be put together as follows

$$\min_{\mathbf{\Delta T}, \mathbf{\Delta \alpha}, s} J_{QP}\left(\mathbf{\Delta T}, \mathbf{\Delta \alpha}, \mathbf{s}\right) \tag{4.21}$$

subject to

$$\mathbf{B}(\boldsymbol{\alpha}_{prev})\mathbf{\Delta T} + \frac{\partial}{\partial \boldsymbol{\alpha}}(\mathbf{B}(\boldsymbol{\alpha})\mathbf{T})\Big|_{\substack{\boldsymbol{\alpha}=\boldsymbol{\alpha}_{prev} \\ \mathbf{T}=\mathbf{T}_{prev}}} \cdot \mathbf{\Delta \alpha} + \mathbf{s} = \boldsymbol{\tau}_c - \mathbf{B}(\boldsymbol{\alpha}_{prev})\mathbf{T}_{prev} \tag{4.22}$$

$$\mathbf{\Delta T}_- \leq \mathbf{\Delta T} \leq \mathbf{\Delta T}_+ \tag{4.23}$$

$$\mathbf{\Delta \alpha}_- \leq \mathbf{\Delta \alpha} \leq \mathbf{\Delta \alpha}_+ \tag{4.24}$$

$$\mathbf{s}_{min} \leq \mathbf{s} \leq \mathbf{s}_{max} \tag{4.25}$$

The optimization problem (4.21) - (4.25) was solved by using the QLD solver by Schittkowski (1986). The QLD solver is a well tested algorithm for solving QP problems.

4.3 Proposed Control Allocation Algorithm

4.3.1 Forbidden Sectors

To try to reduce the effects of common thruster losses (as described in section A.3.2) forbidden thrust production zones are introduced as done in Ruth (2008). The forbidden zones tries to prevent thruster to thruster interaction and the Coanda effect for Cybership III. The forbidden thrust production zones, which are the same used by Ruth (2008), can be viewed in Figure 4.2 below

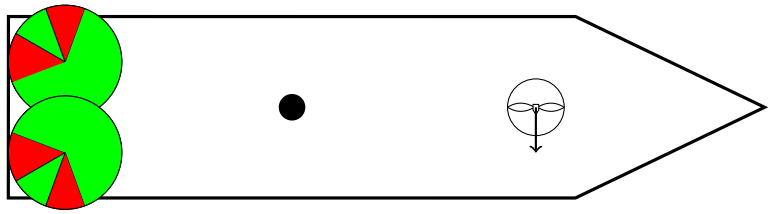

Figure 4.2: CyberShip III Forbidden Thrust Production Zones

The problem with forbidden sectors is that the solution in the subset $\alpha_j \subset [-180°, 180°]$ is non-convex. Convexity is a necessary to have a feasible solution in quadratic programming as mentioned earlier. To regain convexity the problem is divided into several sectors which is individually convex as has previous been done in Johansen et al. (2003, 2007) and Ruth (2008). The large green sectors of the stern pods has to be diveded into two smaller sectors as it is not convex otherwise. The sectors chosen for the stern pods is the same as implemented in Ruth (2008) where there is an overlap between the different sectors. The different sectors and their values can be seen in Table 4.1. The overlap between sectors is implemented to reduce the switching between neighboring sectors. The switching algorithm will be discussed in section 4.3.2

Sector number	α_1 [deg]	α_2 [deg]	α_3 [deg]
1	[90]	[-109, 70]	[-70, 109]
2	[90]	[-109, 70]	[-20, 159]
3	[90]	[-109, 70]	[-150, -110]
4	[90]	[-159, 20]	[-70, 109]
5	[90]	[-159, 20]	[-20, 159]
6	[90]	[-159, 20]	[-150, -110]
7	[90]	[110, 150]	[-70, 109]
8	[90]	[110, 150]	[-20, 159]
9	[90]	[110, 150]	[-150, -110]

Table 4.1: Sector division as seen in Figure 4.2. α_1, α_2 and α_3 is the azimuth angles for bau azimuth, stern starboard pod and port pod respectively

4.3.2 Supervisory Control Allocation

As the solution has been split into several sectors, each with their individual constraints on azimuth angles an algorithm is needed to select the appropriate sector based upon design choices. Switching between sectors will solve the issue with nonconvex problems, as each individual sector is convex. In this thesis a supervisory controller (supervisor) is responsible to select which sector to use. The theory to design a supervisor controller are found in Hespanha et al. (2003). As nonlinear systems can be unstable if operating conditions are changed rapidly, as this can lead to rapid change stabilization points; Khalil (2002), it was proposed in Hespanha et al. (2003) to introduce hysteresis switching and dwell time switching in the supervisor. Examples of supervisory controller in marine vessel controllers can be found in Nguyen et al. (2007, 2008).

The switching in the supervisor will exploit each sectors potential to reduce the total consumed power amongst the thrusters. This includes both monitoring the total potential sector consumption and how close to fulfilling the goal of keeping $\mathbf{B}(\boldsymbol{\alpha}_d)\mathbf{T}_d - \boldsymbol{\tau}_c$ as small as possible. The latter is needed as some solution might not produce any thrust, and

thus have no power consumption and seems like a good solution. But such solutions will not solve the main goal of allocating the commanded generalized force from the controller.

The iterative solution of the supervisory control allocation

The supervisory control allocation used in this thesis will be solved by the following steps

1. Solve each sector to find an appropriate angle and thrust based on previous step solution.
2. Based upon each sector's solution on thrust setpoint $\mathbf{T}$ and slack variables s the supervisor will find the appropriate sector to be used.
3. Once the sector solution is chosen another QP-solver is activated. This QP-solver takes the angle solution from the appropriate sector and solves the problem for $\mathbf{T}$.

Sector Control Allocation Solution

As the previous azimuth angle can impossibly be every sector at once the potential for one sector's power reduction potential might be unnoticed in the supervisor. This is due to the direction of the thrusters are potentially outside the sector angle constraints. Even though (4.20) allows the angles and thrust to be outside the sector limits, the calculated α_+ still might not be within sector limits. $\boldsymbol{\alpha}_{sec}$ is calculated for each individual sector.

It is proposed here to do a slight modification to how the constraints in (4.24) are calculated. Instead of calculating $\boldsymbol{\Delta\alpha}_{+/-}$ using $\boldsymbol{\alpha}_{prev}$ a new angle $\boldsymbol{\alpha}_{sec}$ is proposed. $\boldsymbol{\alpha}_{sec}$ will be equal to $\boldsymbol{\alpha}_{prev}$ if it is within the azimuth angle constraints $\boldsymbol{\alpha}_{max}$ and $\boldsymbol{\alpha}_{min}$. If not, $\boldsymbol{\alpha}_{sec}$ will be equal to $\boldsymbol{\alpha}_{max}$ or $\boldsymbol{\alpha}_{min}$ depending on which is closest.

The constraints (4.19c), (4.19d), (4.20c) and (4.20d) is then modified with $\boldsymbol{\alpha}_{sec}$ as follows

$$\boldsymbol{\Delta\alpha}_{+} = \boldsymbol{\alpha}_{+} - \boldsymbol{\alpha}_{sec} \tag{4.26a}$$

$$\boldsymbol{\Delta\alpha}_{-} = \boldsymbol{\alpha}_{-} - \boldsymbol{\alpha}_{sec} \tag{4.26b}$$

$$\boldsymbol{\alpha}_{+} = \max\left(\min\left(\boldsymbol{\alpha}_{max}, \boldsymbol{\alpha}_{sec} + \dot{\boldsymbol{\alpha}}_{max}\Delta t\right), \boldsymbol{\alpha}_{sec} - c_1\dot{\boldsymbol{\alpha}}_{max}\Delta t\right) \tag{4.26c}$$

$$\boldsymbol{\alpha}_{-} = \min\left(\max\left(\boldsymbol{\alpha}_{min}, \boldsymbol{\alpha}_{sec} - \dot{\boldsymbol{\alpha}}_{max}\Delta t\right), \boldsymbol{\alpha}_{sec} + c_1\dot{\boldsymbol{\alpha}}_{max}\Delta t\right) \tag{4.26d}$$

With these constraints the solver in (4.21)-(4.25) will be run for each sector.

Supervisor

After each sector has calculated the potential azimuth angle and thrust the supervisor will be activated. The supervisor inputs are the thrust setpoints $\mathbf{T}$ and the slack variables $\mathbf{s}$.

Hysteresis and dwell time switching is implemented in the supervisor according to Hespanha et al. (2003). The hysteresis effect is both in power and sum of slack variables. The hysteresis effect in power is to prevent to switch unnecessary switching to sectors which are barely more power efficient to the previous. The hysteresis effect in the sum of slack variables is to prevent switching to sectors that is more power efficient at the cost of much higher sum of slack variables. An example of this would be if $\boldsymbol{\tau}_c = [3, 0, 0]$ is set as input to the control allocation, and some of the sectors pointing backwards would have the solution $\mathbf{T}_d = [0, 0, 0]$, i.e no power, but the sum of slack variables would be $\mathbf{s}_{sum} = 3$. This would not be an optimal solution.

In this thesis the total logic behind the supervisor is as follows:

Step 1: Calculate the power in each sector using the power to thrust relationship (A.7). And calculate the sum of slack variables for each sector.

Step 2: Sort the sectors based on minimum sum of slack variables.

Step 3: Find the best sector of the 4 best sectors based on minimum slack variables and power from step 2. The best sector is found by looping

over each of the 4 best sectors starting with the one with minimum slack variables and check if the other 3 sectors has less power without increasing the slack variables too much (hysteresis effect). In this thesis it was found that an increase of 5% in the sum of slack variables was a value that worked well, as long as the power decreased.

Step 4: Based upon the best sector, I_s, found in Step 3 we have the following selection criteria based upon Ruth (2008) and Hespanha et al. (2003)

$$I = \begin{cases} I_s, & \text{if } t > t_{lim} \wedge (P(I_s) < (P(I_p) - P_{lim}) \\ & \qquad \wedge (S(I_s) < (1 + s_{lim}) \cdot S(I_p) \\ I_o, & \text{if } t < t_o \wedge I_s = I_o \\ I_p, & \text{otherwise} \end{cases} \tag{4.27}$$

where t is the time between the last switch. t_{lim} is the dwell time switching. $P(\cdot)$ and $S(\cdot)$ is the power and sum of slack variables to specific sector respectively. P_{lim} and s_{lim} is the hysteresis limit for the power and sum of slack variables respectively. P_{lim} is in Newton, while s_{lim} is in percentage. As mentioned earlier $s_{lim} = 5\%$ was a value that worked good, and will be used in this thesis. I_p is the previous sector, while I_o is the selected sector before I_p. In case $I_s = I_o$ and $t < t_o$ the the sector I_o will be chosen. This is a precaution to prevent a switch to another sector due to transient behavior in $\boldsymbol{\tau}_c$ which will favor another sector for a short period. $t_o < t_{lim}$ and should be small enough to prevent these transient behaviors. $t_o = 1s$ was a value that worked well as the thrusters has limited time to rotate in this time span due to rate constraints.

Solve T for given alpha

Once a specific sector has been chosen the appropriate change in alpha from the selected sector must be calculated. As the azimuth rate change solution from the sector, denoted here as $\boldsymbol{\Delta\alpha}_{sec}$, is based upon the angle

$\boldsymbol{\alpha}_{sec}$ a transformation to rate change relative to the previous angle is needed. This is done as follows

$$\boldsymbol{\alpha}_{diff} = \boldsymbol{\alpha}_{sec} + \boldsymbol{\Delta\alpha}_{sec} - \boldsymbol{\alpha}_{prev} \tag{4.28}$$

Then $\boldsymbol{\alpha}_{diff}$ is mapped to the domain $[-\pi, \pi]$, as the difference might be higher than $\pm\pi$, by using a $-$[inf, inf] to [$-$pi, pi] block in the MSSToolbox (2012). After the mapping the difference is rate saturated according to the maximum allowed change in (4.20). The rate saturated angle is then the new change in azimuth angle, $\boldsymbol{\Delta\alpha}_{new}$, to be used to solve the allocation problem for the thrust setpoints.

The lower and upper bound for azimuth change in the solver (4.21)-(4.25) is then

$$\boldsymbol{\Delta\alpha}_{-} = \boldsymbol{\Delta\alpha}_{+} = \boldsymbol{\Delta\alpha}_{new} = \boldsymbol{\Delta\alpha} \tag{4.29}$$

Since the angle is fixed in this problem, (4.21)-(4.25) can be modified to reduce the computation such as removing the singularity avoidance.

Setpoints to the thrusters

Once the allocation problem has been solved the new setpoints to the thrusters is as follows

$$\mathbf{T}_d = \mathbf{T}_{prev} + \boldsymbol{\Delta T} \tag{4.30}$$

$$\boldsymbol{\alpha}_d = \boldsymbol{\alpha}_{prev} + \boldsymbol{\Delta\alpha} \tag{4.31}$$

Chapter 5

Simulation Study

Simulation study will consist of the following cases

S1 Simple control allocation using constant commanded generalized force.

S2 Full sea state testing of the supervisory control allocation. Includes a power-efficiency comparison to a pseudo-inverse control allocation solution.

S3 Testing of the singularity avoidance scheme added to the supervisory control allocation in the cost function.

The purpose of the simulation case 1 is to present the inner workings of the proposed supervisory control allocation.

Simulation case 2 is a simulation with all the environmental forces activated as described earlier. A Moore-Person pseudo-inverse control allocation is also tested with the purpose to test the power-efficiency of the supervisory control allocation.

Simulation case 3 tests the singularity avoidance scheme in (4.15), if the sufficient spread of the stern pods are achieved on CyberShip III.

5.1 S1: Simulation Case 1

This simulation case will take into account how the supervisory control allocation algorithm proposed in Chapter 4 performs with a switch in commanded generalized thruster force. The input will switch from $\boldsymbol{\tau_c} = [3, 0, 0]^T$ to $\boldsymbol{\tau_c} = [-3, 0, 0]^T$ at $t = 100s$. This test is only including the supervisory control allocation without any thruster dynamics.

5.1.1 Results and discussion

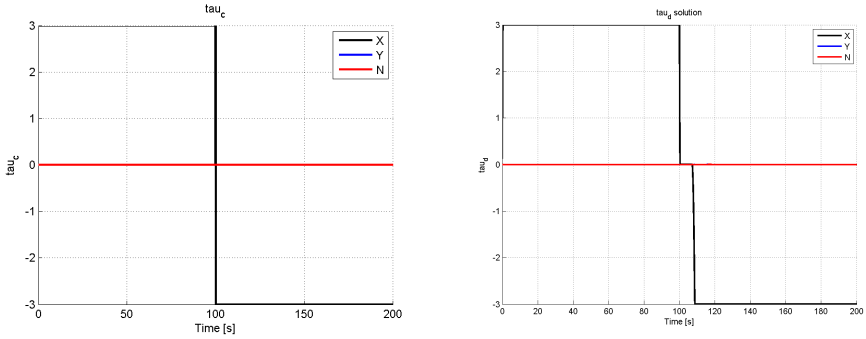

(a) Step force input to the control allocation problem

(b) Force solution to step force input to allocation problem

Figure 5.1: Input and solution to the supervisory control allocation with force input

In Figure 5.1b it can be seen that the force solution lags behind force input in Figure 5.1a. This is due to the rate constraints to the stern pods onboard Cybership III. This effect can be seen on the figures 5.2 and 5.3. The effect of the singularity avoidance can clearly be seen in Figure 5.3 in the time span $t \subset [0s, 100s\rangle$, where the azimuth angle for the stern pods is not 0, but spread out in different direction to gain manoeuvrability. Once the switch from $X = 3\ [N]$ to $X = -3\ [N]$ the thruster forces goes down to zero as the angles for the pods are pointing forwards as the optimization wants to minimize both the power and the correctness of the force input. As the thruster force reduces to zero the angles for the

pods are rotating. Once the pods has sufficient angle to produce force in the correct direction they start to spin up, as can be seen in Figure 5.2 at $t = 110s$. The new sector constraints α_{max} and α_{min} in Figure 5.3 is also shown as better sectors are chosen. As the angle of the pods starts to get more favourable the thruster force reduces to reduce the power which can be seen in Figure 5.4. From Figure 5.3 it is also shown that the pods swipes through the illegal thrust production zones between sector 9 and sector 5 in the Table 4.1 as they are allowed to do this due to (4.20). Another thing that should be noted is that the solution based upon negative X-force has increased power consumption than with positive X-force input (as seen in Figure 5.4), but the increase in power is due to it is not allowed to produce thrust in the forbidden thrust production zones.

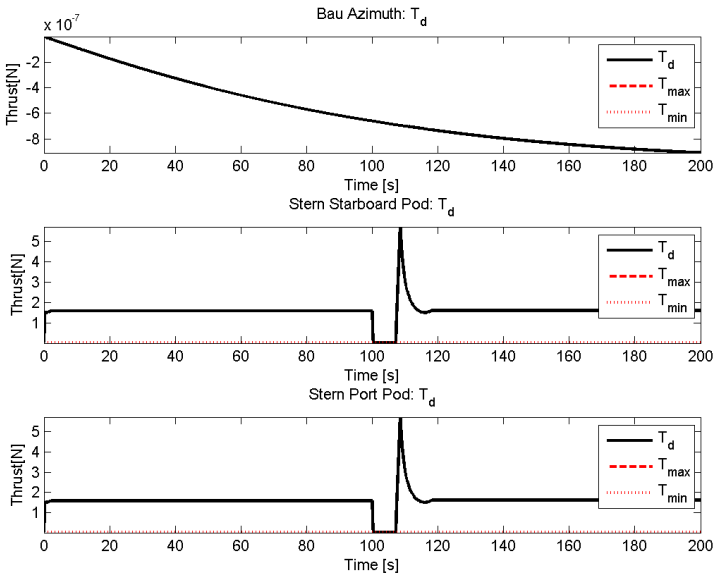

Figure 5.2: Desired thruster force solution to the control allocation problem for step force input

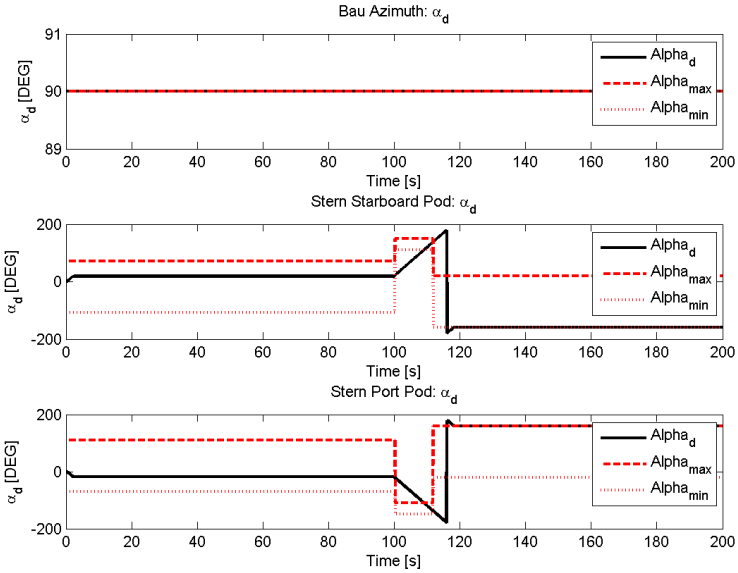

Figure 5.3: Desired azimuth angle solution to the control allocation problem for step force input with current sector constraints

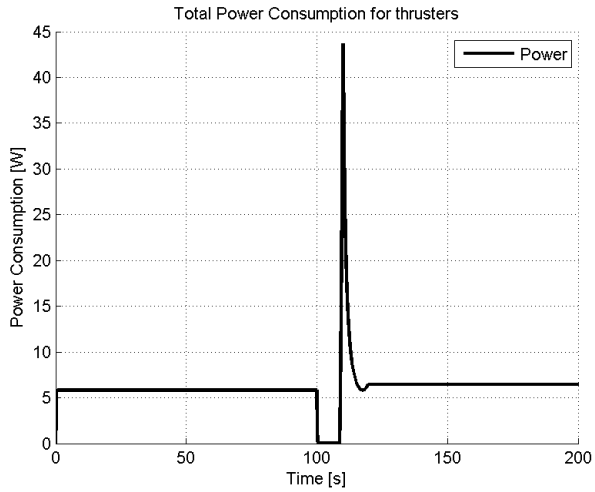

Figure 5.4: Total thruster power consumption for step force input

The supervisor solution to the best suited sector for the given input can be found in Figure 5.5. As can be seen from the Figure 5.5, sector 9 is redeemed the best sector at $t = 100s$ when the switch in force input happens. However, as the thrusters starts to rotate a better solution in sector 5 is found. This has to do with which of the closets azimuth angle constraints are for both sector 9 and 5. The power potential calculated by the supervisor at $t = 100s$ was $P_9 = 3.4855W$ and $P_5 = 5.8423W$ for sector 9 and 5 respectively. While at $t \approx 115s$ the potential was $P_9 = 7.2230W$ and $P_5 = 6.4534W$, so sector 5 is chosen over sector 9 as seen in Figure 5.5. Some of the other sectors had much better potential minimum power, but these solution traded thrust to high increase in slack variables compared to sector 9 and 5 and was thus not considered by the supervisor.

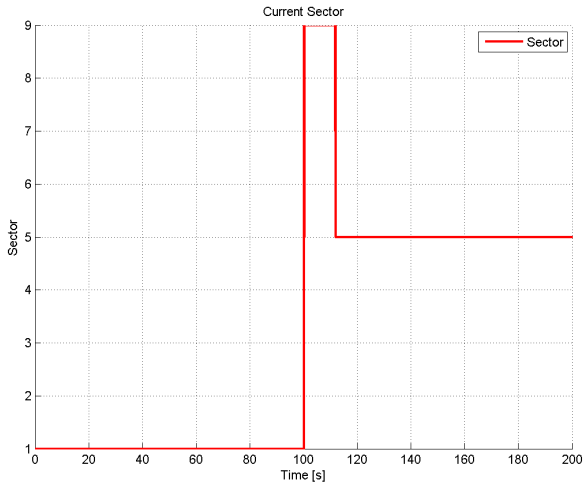

Figure 5.5: Supervisory sector solution for step force input

5.1.2 Conclusion

The supervisory control allocation does successfully reduce power in the system by changing to more optimal operating sectors. The supervisor prevents to jump to sectors that does not produce any thrust to gain no

power consumption by monitoring both the potential power and slack variables to each of the sectors. It was also successfully shown that if a better sector was found where an illegal thrust production zones existed between the previous best sector and the new the solution would swipe as fast as it could through it and prevent to high thruster losses. The error between the input and output generalized force was reduced to zero as the thrusters rotated to angles where this was possible. This was to be expected as there are no thruster dynamics to incorporate the losses.

5.2 S2: Simulation Case 2

The purpose of this simulation case is to test the supervisory controller with full vessel dynamics and environmental forces, and compare it to a different solution to the control allocation problem. It was chosen to compare the supervisory control allocation to an explicit solution, such as the pseudo-inverse described in section 1.3.1.

The control allocation parameters can be found in section C.1. Pseudo-inverse control allocation used was the Moore-Penrose pseudo-inverse (1.4), with the weight $\mathbf{W} = \mathbf{I}$. For the pseudo-inverse control allocation the bau azimuth was set to 90° similar to the supervisory control. While the stern pods angles was found by conducting several simulation tests, not included here, to find the most power efficient angle for the given environmental loads. The angle found for the stern pods was $\pm 15^\circ$.

The DP-controller was set to the following values

$$K_p = \text{diag}\{[10,\ 3,\ 30]\} \tag{5.1}$$
$$K_d = \text{diag}\{[30,\ 30,\ 100]\} \tag{5.2}$$
$$K_i = \text{diag}\{[0.1,\ 0.4,\ 2]\} \tag{5.3}$$

The main environmental particulars was as follows

- Current
  - Velocity = 0.05 [m/s]

  - Mean direction = $190°$
- Waves
  - Hs = 0.06 [m]
  - ω_0 = $180°$
  - Mean direction = $180°$
- Wind
  - $u_{10} = 0.5$ [m/s]
  - Mean direction = $180°$

The detailed environmental data can be found on the DVD in the file "Parameters.m".

5.2.1 Results

Pseudo Inverse

The position and heading results can be viewed in Figure 5.6 as the red/blue color. A north-east position results of Figure 5.6 can be found in the Figure D.1. A drift-off is detected at the start of the simulation at $t = 0[s]$, which can be seen both in x and y position in the figures 5.6 and D.1. At $t \approx 15[s]$ the drift-off is approximately 0.15 [m], which is 3 meters in the full supply vessel scale of CyberShip III. The position and heading starts to converge after an initial time to the desired reference of $x = 0$, $y = 0$ and $\psi = 0$ marked as black in the figures. However, the solution do oscillates around the desired position and heading.

Thruster forces can be viewed in Figure 5.7. Black and red colors denotes desired and actual thrust force for each individual thruster onboard CyberShip III. Thruster angles plot is not included as they are fixed in the pseudo-inverse control allocation. The resulting body-framed 3-DOF force and moment from the thrust and angle of the thrusters can be viewed in Figure D.2. The Black, blue and red colors represents the desired, commanded and actual forces and moment respectively.

Power consumption for the pseudo-inverse can be viewed in Figure 5.11 as the red color.

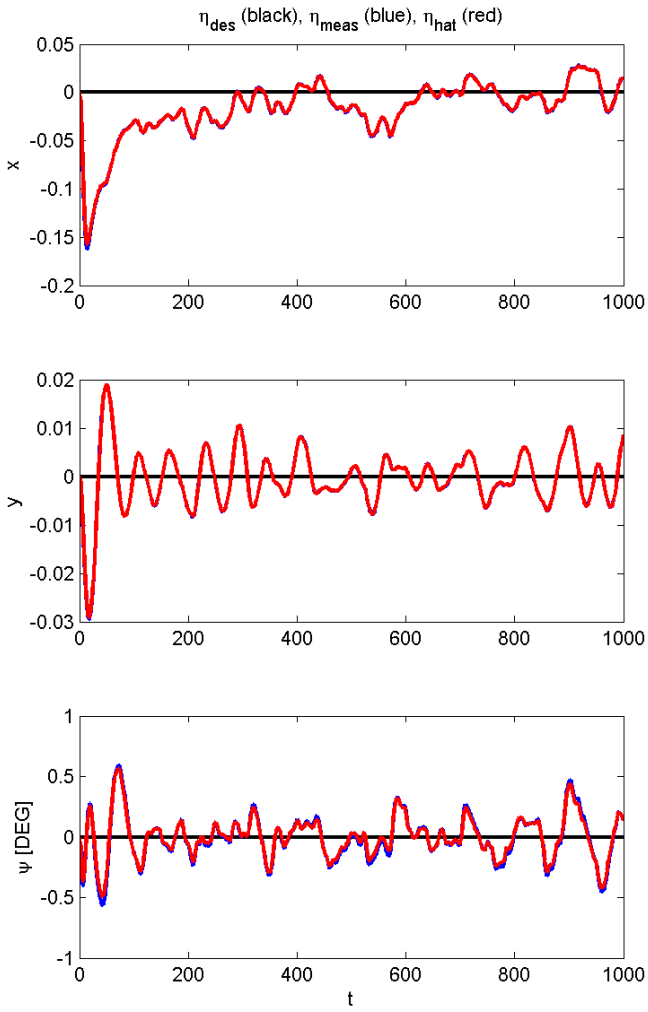

Figure 5.6: Simulation Case 2 - Pseudo-inverse: Position and heading results

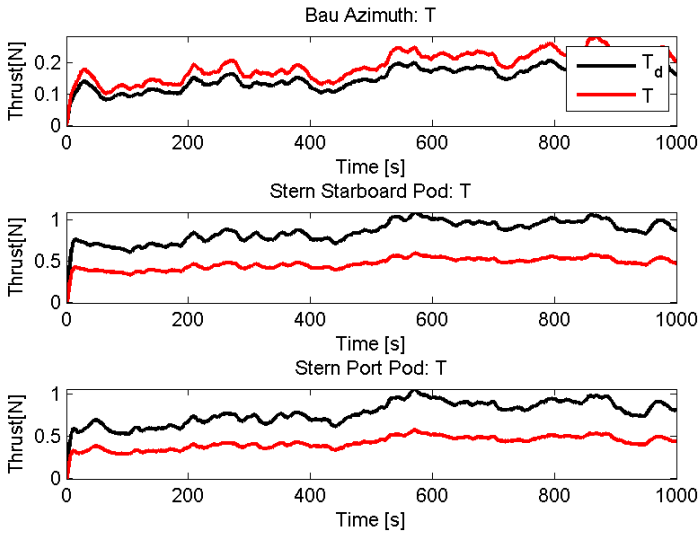

Figure 5.7: Simulation Case 2 - Pseudo-inverse: Desired (black) and actual (red) thrust production

Supervisory Control Allocation

Position and heading results can be viewed in Figure 5.8. The desired position and heading is equal to the Pseudo-Inverse simulation test ($x = 0$, $y = 0$ and $\psi = 0$ marked as black). In Figure 5.8 the desired position and heading is marked as black, measurements as blue and estimated as red. The North-East equivalent of Figure 5.8 is found in Figure D.5. As detected in the simulation of the Pseudo-Inverse a drift-off is detected in the beginning of the simulation, with a peak of about $0.16[m]$ in the x-direction. After the initial drift-off the position of the vessel moves towards the desired position. However, similar to the Pseudo-Inverse the resulting position of the vessel does oscillate around the desired position and heading. The oscillations does not exceed ± 0.05 [m] after $t = 200$ [s] in the x-direction. Y-direction and heading oscillations are also very low, with ± 0.01 [m] and $\pm 0.5^{\circ}$ after $t = 200$ [s]. Environmental loading acted on CyberShip III during this simulation test can be viewed in the

figures D.8 and D.9.

Results of the different thrusters for the supervisory control allocation can be seen in the figures 5.9 and 5.10. As can be seen from Figure 5.9 the desired thrust for the stern pods is higher than the actual produced thrust. While for the bau azimuth the desired thrust is lower than the actual produced thrust. The azimuth angle for the bau thruster is fixed at 90° and thus is expected to remain in this position as can be seen in Figure 5.10. While for the starboard stern pods we can see that it rotates to the region $110^\circ - 150^\circ$ after $t \approx 40[s]$. The port stern pod hovers around $5^\circ - 7^\circ$. Resulting force in body-frame from the thrusters can be seen in Figure D.6, while the difference between the commanded and desired generalized force can be viewed in Figure D.7 in black color. Slack variables used in the control allocation algorithm can also be seen as the red color in Figure D.7.

The estimated power consumption by the thrusters in the supervisory control allocation can be seen in Figure 5.11 as the black color.

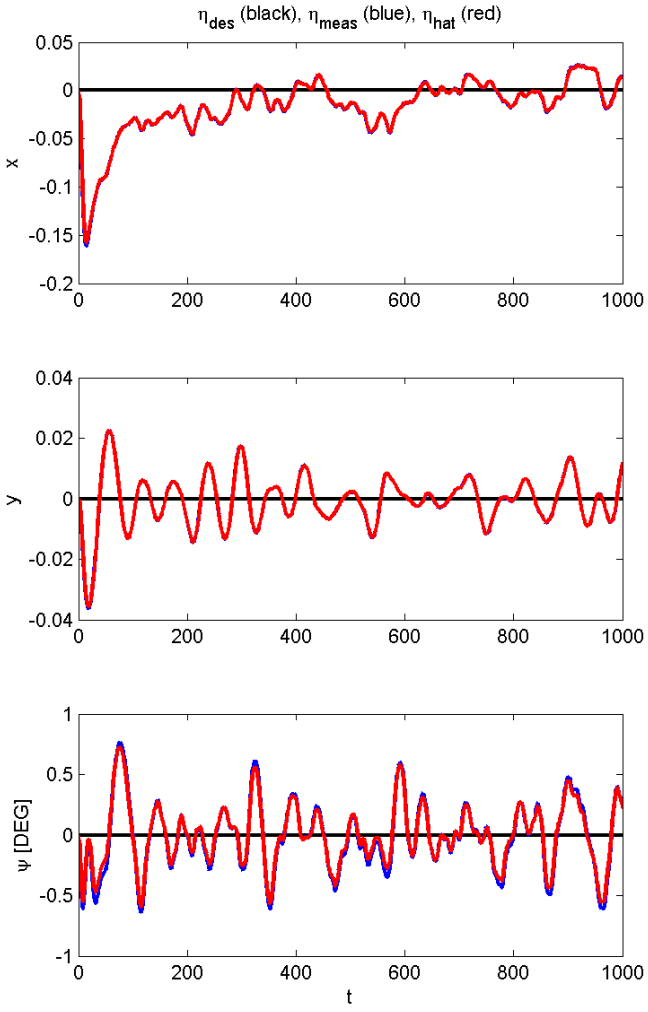

Figure 5.8: Simulation Case 2 - Supervisory Control Allocation: position and heading results

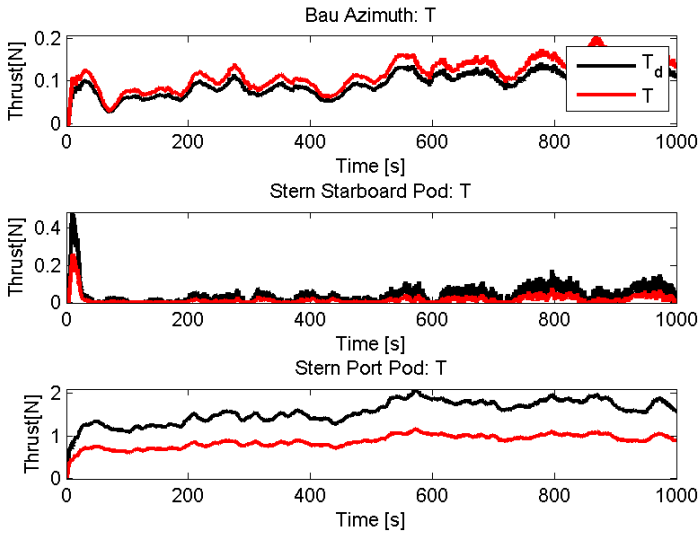

Figure 5.9: Simulation Case 2 - Supervisory Control Allocation: Desired (black) and actual (red) thrust production for the different thrusters onboard CyberShip III

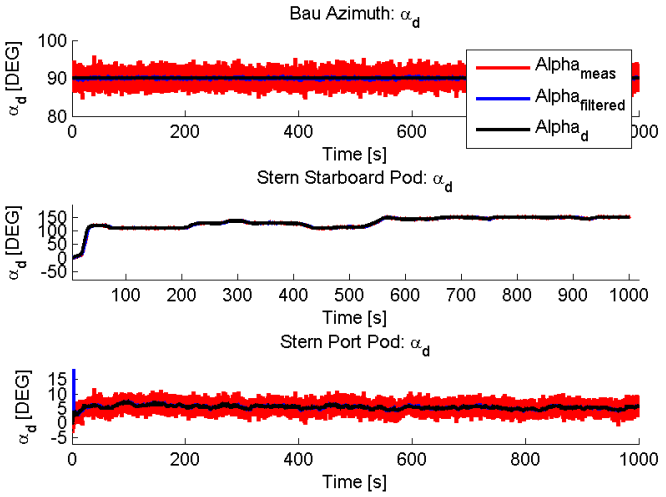

Figure 5.10: Simulation Case 2 - Supervisory Control Allocation: Measured (red), filtered (blue) and desired (black) thruster angles

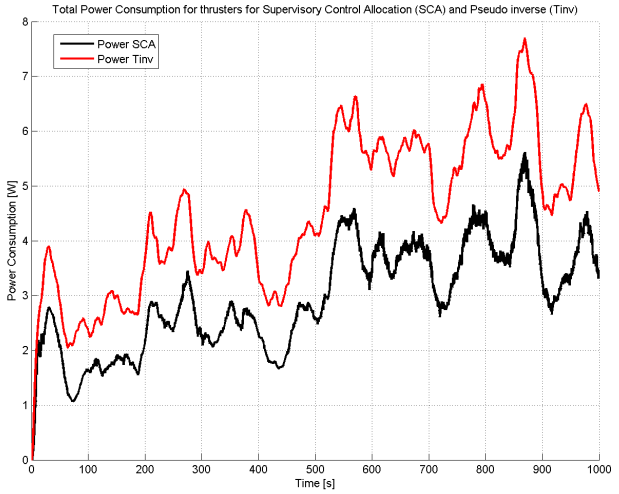

Figure 5.11: Simulation Case 2: Estimated power consumption for Supervisory Control Allocation (black) and Pseudo-Inverse (red)

5.2.2 Discussion

Drift-off experienced in both the simulation tests of pseudo-inverse and supervisory control allocation, in the figures 5.6 and 5.8, is due to the initial environmental loads are not taken into account in the controller. It is not before a sufficient position and heading error has occurred that the controller starts counter-acting the environmental loads in an acceptable degree. The controller must not only counter-act the position error but also the initial velocity the vessel has in the beginning of the simulation. The initial velocity of the vessel could have been compensated for in the reference model, thus making the derivative part of the PID-controller to calculated a force opposite of the initial velocity. Position in x-direction particular, in the figures figures 5.6 and 5.8, is quite slow moving. The slow movement in position of the vessel is due to the high derivative part of the PID-controller, making rapid movement non-desired. Reason for the non-desired rapid movements was to especially reduce rapid changes in the heading, as this would cause the environmental loads to change direction relative to the vessel at a higher rate and thus make the loads more unpredictable. Another reason for the lack of faster movement of the vessel is due to thruster dynamics, since increased advance speed changes thrust characteristics (Figure 3.5) as was seen in the figures D.2 and D.6. The difference between these two figures and the effect of thruster dynamics will be discussed later.

Thruster angles for the pseudo-inverse was stable at $\boldsymbol{\alpha} = [90°,\ 15°,\ -15°]$. If this was not the case the pseudo-inverse solutions would be wrong. Angles solution found for the supervisory control allocation varied a lot in local region as explained in the results section. As seen in Figure 5.10 the stern port pod solutions lied around $5° - 7°$ to align it self towards the environmental forces in the figures D.8 and D.9. While the stern starboard pod angle solution was in the region $110° - 150°$ after $t = 40[s]$. The main reason for these particular regions for the stern pods is due to power-efficiency. The bau azimuth has a much worse thrust-to-power relation than the stern pods, as the table 3.3 and (3.29) shows. As what can then be seen in the thrust production in figure 5.9 is that all of the force in surge is produced by the stern port pod. Both the stern port pod and starboard pod is set such that

they both produce positive sway force and moment easing the load on the bau azimuth. Compared to the load on the bau azimuth in the pseudo-inverse solution (Figure 5.7) and the supervisory control allocation solution (Figure 5.9), we can see that the latter has lower load on the bau azimuth than the former.

It was noted that the actual thrust produced and the desired thrust for both simulation tests were not equal, as noted in the figures 5.7 and 5.9. The reason for the difference is the use of the reverse mapping in (3.28) with the data in table 3.2. The reverse mapping used will increase the shaft speed compared to the simulated thrust production for the propellers in (3.23), as explained in section 3.7. The actual produced will then be higher than desired thrust, as can especially be seen in the thrust production of the bau azimuth. However, we can see that both the stern pods produce lower thrust than the desired thrust. The reason for the actual thrust is lower than the desired is due to the thrust calculation in (3.23). Where the thrust production is highly dependable on the advance velocity (A.8) and the thrust thrust characteristics in Figure 3.5.

Correctness of the control allocation for pseudo-inverse and supervisory control allocation can be viewed in figures D.2 and D.6 respectively. Desired generalized force for pseudo-inverse follows the commanded generalized force. The accuracy for the pseudo-inverse is due to the explicit solution (1.4). However, for the supervisory control allocation there is a bit more error between the commanded and desired generalized forces. The detailed difference can be found in Figure D.7. The main error between the commanded and desired generalized forces is the linearization in (4.22). Also the filtered measurement of the thruster angles were used, which lags a little bit behind the actual angles resulting in a slight error in the difference between τ_c and τ_d.

The estimated power consumption in figure 5.11 goes clearly in favor of the supervisory control allocation solutions than the pseudo-inverse solutions. As mentioned in section 1.3, compared to explicit solutions with fixed thruster angles a iterative solution with rotating thrusters will give better results due to the use of the whole azimuth angle range. Having the rotation, the more optimal angle can be found based upon power-efficiency as was done in the supervisory control allocation.

However, the main difference with the supervisory control allocation is the selection of a power-efficient sector which eases the load on the bau azimuth due to its thrust-to-power relation. By increasing the loads on the stern pods and reducing the load on the bau azimuth the power consumption is lowered.

5.2.3 Conclusion

The supervisory control allocation was shown to give a slow and stable solution to gain the desired position and heading as wanted by the design of the controller. The results is kept withing ± 0.15 [m] in x and y. The heading is always withing $\pm 1^\circ$, resulting in a very stable heading towards the mean environmental forces, thus reducing the total power consumption. The solution given by the supervisory control allocation resulted in setting stern starboard pod in the region $110^\circ - 150^\circ$ and the stern port pod about $5^\circ - 7^\circ$. This was to reduce the load on the bau azimuth which was set to an angle of 90°. Since the bau azimuth had a worse thrust-to-power relation the total power was reduced compared to a pseudo-inverse control allocation solution.

5.3 S3: Simulation Case 3

In this section the singularity avoidance (4.15) in the cost function is tested with the same environmental load as simulation case 2. The only difference is the direction of the current, which is set to 180°. The purpose of this test is to see how the resulting thruster angles becomes during an increase of ρ in (4.15).

5.3.1 Results

The resulting thruster angles by starting with $\rho = 0$ and increasing with one decimal point for each simulation test can be found in the figures 5.12- 5.16

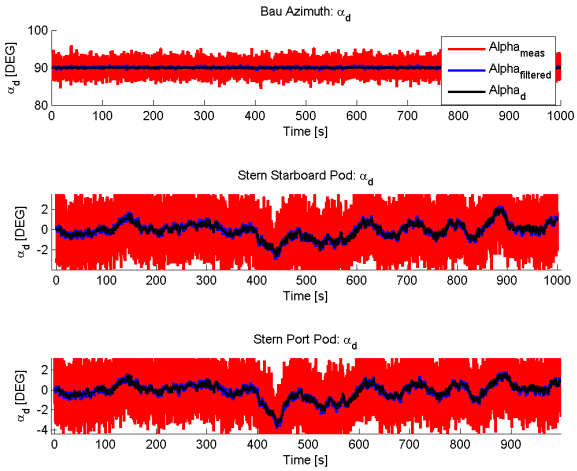

Figure 5.12: S3: Thruster angles results for $\rho = 0.0$ in (4.15)

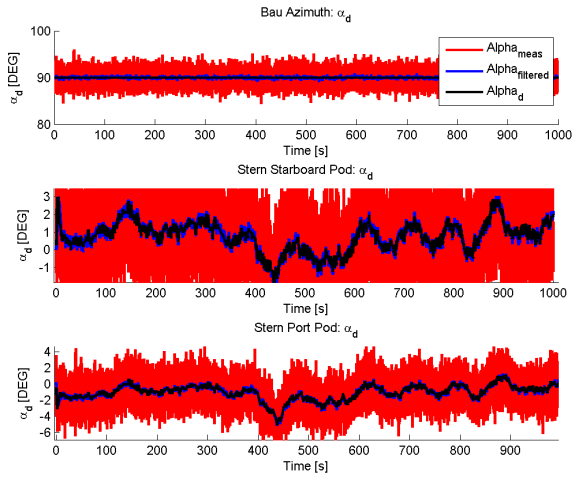

Figure 5.13: S3: Thruster angles results for $\rho = 0.001$ in (4.15)

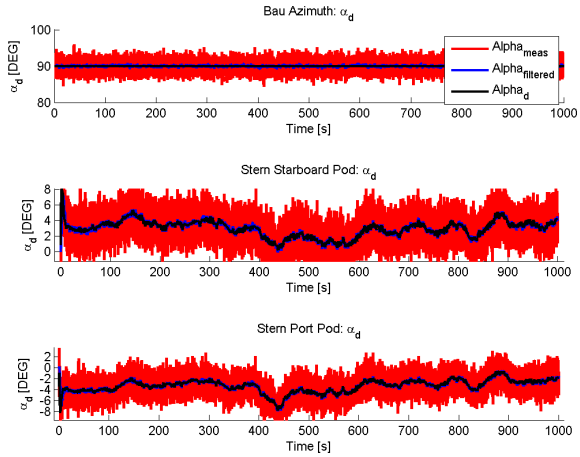

Figure 5.14: S3: Thruster angles results for $\rho = 0.01$ in (4.15)

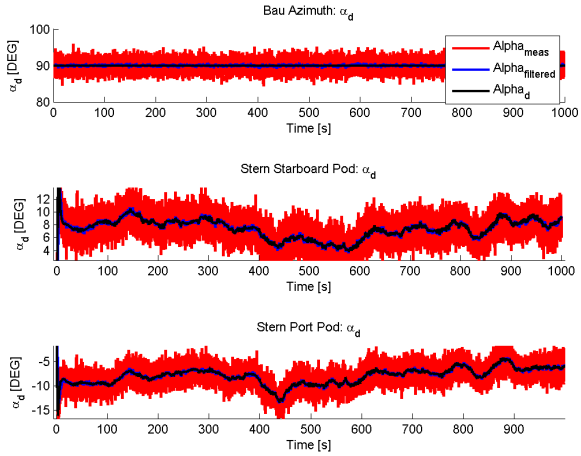

Figure 5.15: S3: Thruster angles results for $\rho = 0.1$ in (4.15)

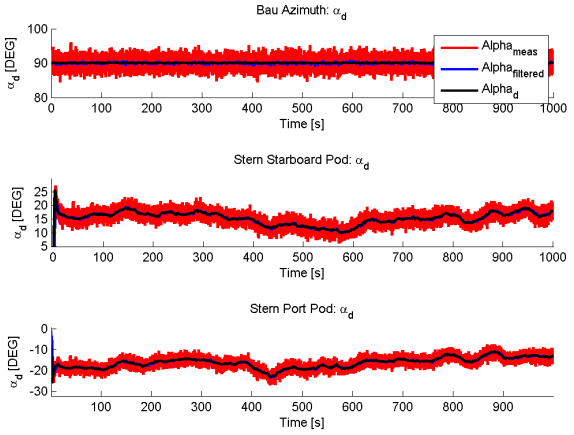

Figure 5.16: S3: Thruster angles results for $\rho = 1.0$ in (4.15)

5.3.2 Discussion and Conclusion

The results in Figure 5.12 does not contain any singularity avoidance, and thus both stern pods varies between positive and negative angles to achieve the most power-efficient solution. The first simulation test containing singularity avoidance is located in Figure 5.13, which also varies between positive and negative angles. It was expected that this should not happen, as this would make the matrix $\mathbf{B}$ close to singular. However, there are two explanations for how this happens. Firstly the singularity avoidance is very weak and does not produce significant cost in the cost function of the quadratic solver. The cost of producing lower power is higher than the singularity avoidance, and thus the latter is ignored to be able to reduce the cost in the cost function. Secondly the code (qld.c) used to solve the problem has a threshold of error in the order of 10^{-9}, so when the parameter ρ which dictates the aggressiveness of the singularity avoidance is small combined with very small thrust angle change (as the angle is in radians) the cost punishment itself is very low and might be ignored in the solver code.

In Figure 5.14 where $\rho = 0.01$ we can see that the stern pods spreads

out to prevent a singular case. Stern starboad pod only has positive angles in the region around 3°. Stern port pod is similar to the starboard pod, only with negative angles. Only when the port pod goes sufficient down to about -8° the starboard pod comes close to 0°, resulting in a decent spread between the pods to gain non-singular case. Had the forces been higher than currently acted on the vessel the spread would be smaller. This could have been counteracted with having a larger singularity avoidance parameter ρ as in the figures 5.15 and 5.16 as these have higher spread between the pods. Both the results in the figures 5.15 and 5.16 has similar results to Figure 5.14 only with higher spread, and will not be discussed further here.

It was here in this simulation case shown that the singularity avoidance works in spreading out the stern pods to prevent singular problems. However, as noted if a higher force was acted on the vessel the spread between the pods would be smaller. This problem could maybe be fixed by having a dynamic singularity avoidance instead of a static parameter chosen here in this thesis. And instead calculate the parameter ρ for each time step for individual forces acted upon the vessel. But the problem with singularity is that the force acted upon the vessel might be sudden and make the vessel drift from its desired position and heading, and an estimator might not be able to predict such sudden force. Such a dynamic solution might then be wanted.

Chapter 6

Experimental Study

6.1 Preliminaries

There was experienced high noise on the azimuth angle measurement onboard Cybership III. Also at certain angles the measurements started to jump 20° or more. This was especially detected around 180°. A method to exclude any large jumps was implemented, but in some cases the angle measurement could start to drift in one direction for a smaller time period and thus become undetected.

Due to the measurement issue with the angle, the angles used in the sector analysis in section 4.3.2 is the previous allocated angle instead of measurement (It was also detected that when the measurement were used in the desired angle calculation, the rotation from 0 to 180 degrees went from 18 seconds to 35-45 seconds). However, the measurements are used when the force setpoints for the thrusters are being calculated.

The PID-controller has the following values in this section:

$$K_p = \text{diag}\{[2,\ 0.5,\ 10]\} \tag{6.1}$$
$$K_d = \text{diag}\{[10,\ 10,\ 100]\} \tag{6.2}$$
$$K_i = \text{diag}\{[0.001,\ 0.0001,\ 0.1]\} \tag{6.3}$$

The allocation parameters was set as described in section C.1

6.2 Experimental Test

In this test, irregular waves was implemented using the wavemaker at the MCLab. The waves was implemented by using a PM-spectrum with an full-size wind of 5 meters per second, see Fossen (2011) for spectrum details. Resulting in $H_s = 0.0178$ and $\omega_0 = 0.8$ using Bis-scaling.

ρ in the allocation parameters are set to 0.01.

6.2.1 Results

The position and heading results can be viewed in the Figure 6.1

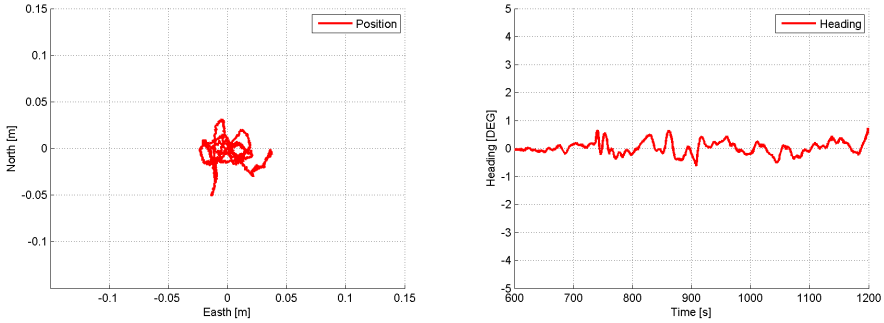

(a) Position results in [m] in the time period $t \in [600,\ 1200]$.

(b) Heading results in [DEG] in the time period $t \in [600,\ 1200]$.

Figure 6.1: Experimental Case 1: position and heading results

In the time span $t \in [600,\ 1200]$, the position of Cybership III is within an error of ± 0.05 both in North and East (x,y). An error of ± 0.05 results to an error of ± 1.5 [m] in full scale vessel. The heading is within $\pm 1^\circ$ in the same time period. Figure 6.2 shows the commanded thrust for the same time span as for the position and heading. Figures 6.3 and 6.4 shows the thrust and angle setpoints for the different respectively. In figure 6.4 the

desired angle is in black and the filtered measurement of the the angle is in red. The allowed thrust production zones are represented as the green areas. The

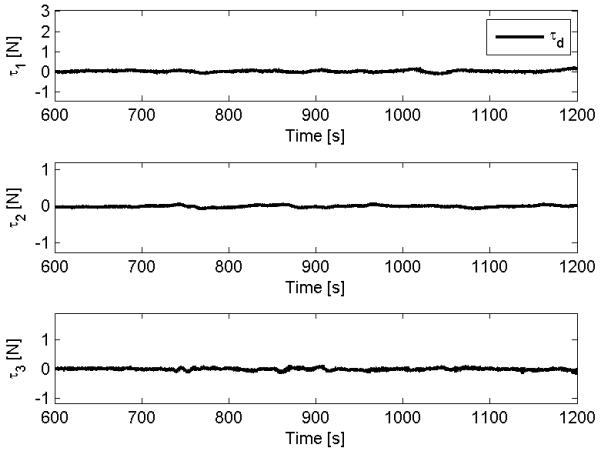

Figure 6.2: The commanded generalized force for the time period $t \in [600,\ 1200]$

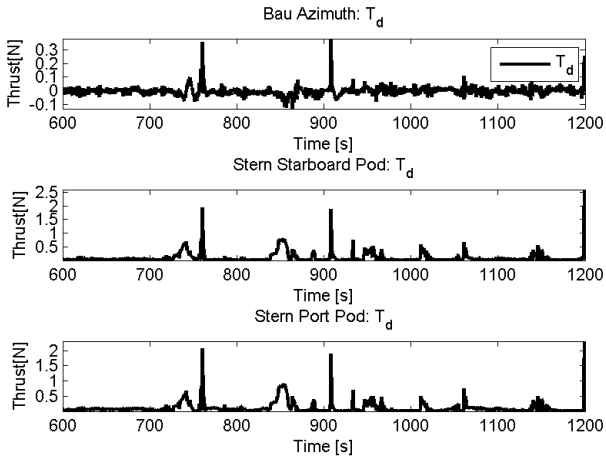

Figure 6.3: Thrusters force setpoints

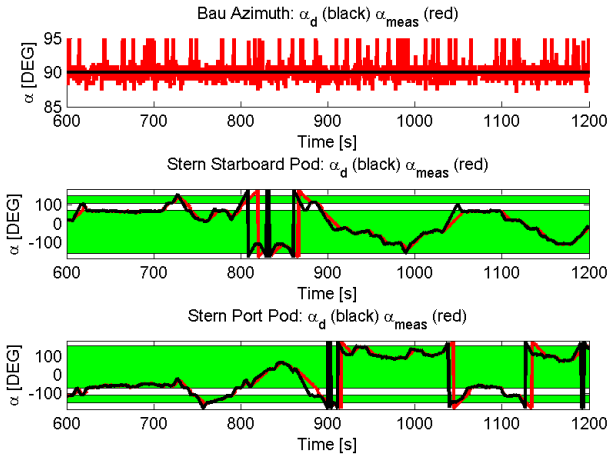

Figure 6.4: Thruster angle setpoints

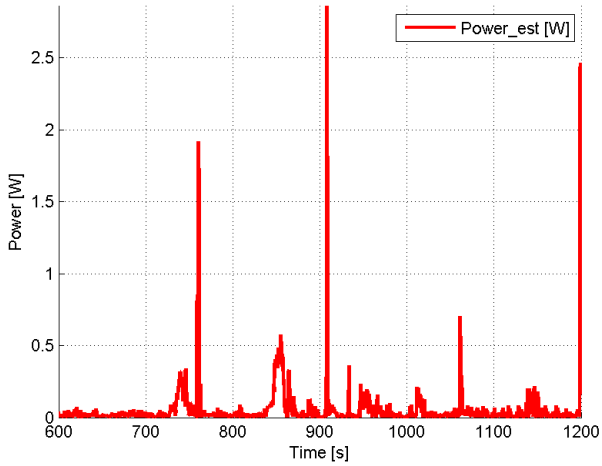

Figure 6.5: Calculated total power consumption of the thrusters onboard Cybership III

6.2.2 Discussion and Conclusion

There was a small issue with the logging of the vessel data on the host pc. Some of the data was logged with different sample time. This difference in sample time made some of the small changes in data to become undetectable in the logged data. Some results was logged with the sample time of 0.25 [s].

The position and heading in Figure 6.1 is very good. The position error in 6.1b was lower than ± 1.5 [m] in full scale. The expected and wanted position error was below ± 3.0 [m]. The heading is aligned directly towards the waves incoming, reducing the load on Cybership III. For DP vessels operating offshore a position error ± 3 [m] should be expected with an heading error of $5°$. The controller was designed to be very passive due to the weight of the vessel of 75kg. The controller had a very high derivative part and low integral part to achieve this. Main reason for the passive controller was to align as best as possible towards the incoming waves.

The angle setpoints does rotate to the most power efficient sectors based upon the control input. In the process the forbidden thrust production zones are avoided by swiping through them as fast as possible, as can be seen in Figure 6.4 where the green areas denotes the allowed thrust production zones. However, there is a lag in the real thruster angles that sometimes get very far behind. This will lead to power efficient sectors being favored from previous allocated angle, and might cause the idea of being in the most power efficient sector not true. Ideally the most power efficient sector should be calculated by the angle measurement. However, as explained in the introduction to this chapter that would lead to an rotation time of $35-45$ seconds instead of 18 seconds. The actual thruster angles will eventually come to the most power efficient sector. The desired thrust reference was calculated with the filtered measurement angle (as explained in the allocation chapter), so the correctness of achieving τ_c is still valid.

We can also see that the setpoints for the pods in Figure 6.3, are much higher than the bau azimuth. This is due to that the power vs thrust is more efficient for the pods than for the bau azimuth. This will lead to that most of the force will be produced by the pods, while the bau azimuth is more used for making small adjustments. Because of the higher use of the pods they will also rotate more to be able to produce the thrust, as was seen in Figure 6.4.

In figures 6.3 and 6.5 there is spikes and build up both in the desired thrust and power. This happens primarily around where one of the pods are close to 180°, and can mainly be explained by the measurement errors around 180 ± 10 degrees for the different thrusters. Around 180 degrees is where the most severe jumps, as explained in the introduction, happens. Since the calculation of τ is using the measurement this will lead to rapid changes. The thrusters onboard Cybership III changes the shaft speed almost instantly, so the rapid changes leads to spikes. Increased thrust setpoints will also lead to that the influence of changing $\boldsymbol{\alpha}$ in the linearization (4.22) increases. As the linearization does not changes the direction of the derivative, when adding $179^\circ + 2^\circ$, this leads to further errors around 180°. If the angle does not change rapidly enough around where the issue is, the error just keeps building up.

Looking apart of the power surges, the supervisory control allocation does what it is suppose to do. It minimizes power, swipes through the forbidden sectors while keeping the position error low.

Chapter 7

Conclusion

The Supervisory control allocation on Cybership III was successfully simulated and experimental tested in the Marine Cybernetics Lab at NTNU.

Three different simulation cases were run to test the potential of the supervisory control allocation. A open loop simulation using a switch in commanded generalized forces were run in Simulation case 1 in section 5.1 to shown the response of the supervisory control allocation algorithm proposed in chapter 4. The test showed that the error between the commanded and desired generalized forces were reduced almost to zero once the thrusters rotated to a favorable position. The power was also minimized by finding the most power efficient sector available. This was done by the supervisor by monitoring the potential for power reduction in each sector while the error between the commanded and desired generalized forces were kept at a minimum. The test also showed that the solution avoided the forbidden thrust production zones implemented in chapter 4. The thrusters swiped through forbidden thrust production if a more power efficient sector was on another side of the current sector. The test also showed that the thrust was evenly distributed amongs the different thrusters based upon their power-efficiency, and punishing the the thrusters with higher thrust setpoint or poor thrust-to-power relation.

In simulation case 2 the supervisory control allocation was tested with full sea state simulation. It was successfully shown that the supervisory control allocation was more power-efficient than a pseudo-inverse control allocation solution by punishing thrusters with poor thrust-to-power relation. The supervisory control allocation also avoided any forbidden thrust production zones while minimizing the power consumption for CyberShip III. The position error was also minimized successfully while the main concern for the supervisory control allocation was the power efficiency.

The additional functionality of singularity avoidance was added to the supervisory control allocation. Simulation case 3 tested the ability to avoid singular cases during a full sea state acted on CyberShip III. Singularity avoidance was achieved by the supervisory control allocation by spreading out the stern pods onboard CyberShip III and was succesfully shown to achieve this goal in the simulation case 3.

The supervisory control allocation onboard the model ship CyberShip III was tested experimentally in the MCLab at MarinTek at NTNU. Waves were created by a wave maker in the pool in the MCLab to create environmental forces. The position of CyberShip III was within an error 1.5 [m] of a full scale supply vessel. The heading were constantly aligned with the incoming waves. The thrusters were successfully avoiding the forbidden thrust production zones, and only swiping through them when necessary. However, it was detected some power spikes and build up when one of the thrusters were close to $180°$. This issue were a combination of measurement errors and linearization errors. Even thought the issues around these angles, the supervisory control allocation minimized the power using the thrust-to-power relation. The bau azimuth, which had very poorly thrust-to-power relation compared to the stern pods, were only used for minor regulation and its use were successfully reduced to lower the power consumption.

Bibliography

Berge, S. P. and Fossen, T. I. (1997). Robust control allocation of overactuated ships; experiments with a model ship. *Preprints IFAC Conference on Maneuvering and Control of Marine Craft*, pages 193–198.

Bernitsas, M. M., Ray, D., and Kinley, P. (1981). Kt, kq and efficiency curves for the wageningen b-series propellers. Technical report, Department of Naval Architecture and Marine Engineering College, The University of Michigan, Ann Arbor, Michigan.

Bodson, M. (2002). Evaluation of optimization methods for control allocation. *Guidance, Control, and Dynamics*, 25:703–711.

Bodson, M. and Frost, S. A. (2011). Control allocation with load balancing. *Guidance, Control, and Dynamics*, 34:380–387.

Bordignon, K. A. and Bodden, W. C. (1995). Closed-form solution to constrained control allocation problem. *Guidance, Control and Dynamics*, 18:1000–1007.

Børhaug, B. (2012). Experimental validation of dynamic capability analysis. Master's thesis, Norwegian University of Science and Technology, Department of Engineering Cybernetics.

Carlton, J. (1994). *Marine Propellers and Propulsion*. Oxford: Butterworth-Heinemann, UK.

Durham, W. C. (1993). Constrained control allocation. *Guidance, Control and Dynamics*, 16:717–725.

Ekstrom, L. and Brown, D. T. (2002). Interactions between thrusters

attached to a vessel hull. In *Proceedings of OMAE'02 - 21st International Conference on Offshore Machanics and Artic Engineering*, Oslo, Norway.

Enns, D. (1998). Control allocation approaches. In *Proc. AIAA Guidance, Navigation and Control Conference and Exhibit, Boston MA*, pages 98–108.

Faltinsen, O. (1993). *Sea loads on ships and offshore structures*. Cambridge University Press, Cambridge New York.

Forssell, B. (2008). *Radionavigation systems*. Artech House Inc., London, reprint of 1991 edition edition.

Fossen, T. (2011). *Handbook of marine craft hydrodynamics and motion control: Vademecum de navioum motu contra aquas et de motu gubernando*. Wiley, Chichester, West Sussex.

Fossen, T. and Johansen, T. (2006). A survey of control allocation methods for ships and underwater vehicles. In *Control and Automation, 2006. MED '06. 14th Mediterranean Conference on*, pages 1 –6.

Fossen, T. I. (2002). *Marine Control Systems: Guidance, Navigation and Control of Ships, Rigs and Underwater Vehicles*. Marine Cybernetics, Trondheim, Norway.

Fossen, T. I. and Sagatun, S. I. (1991). Adaptive control of nonlinear systems: A case study of underwater robotic systems. *Robotic Systems*, 8:393–412.

Frost, S. A. and Bodson, M. (2010). Resource balancing control allocation. In *Proc. American Control Conference*, Baltimore, MD.

Frost, S. A., Bodson, M., and Acosta, D. M. (2009). Sensitivity analysis of linear programming and quadratic programming algorithms for control allocation. In *Proc. of the AIAA Infotech@Aerospace Conference and Exhibit*, Seattle, WA.

Garus, J. (2004). Optimization of thrust allocation in the propulsion system of an underwater vehicle. *International Journal of Applied Mathematics and Computer Science*, 14(4):461–467.

Golub, G. H. and van Loan, C. F. (1983). *Matrix computations*. North Oxford Academic Press.

Hasselman, K., Barnett, T. P., Bouws, E., Carlson, D. E., and Hasselmann, P. (1973). Measurements of wind-wave growth and swell decay during the joint north sea wave project (jonswap). *Deutsche Hydrographische Zeitschrift*, 8(12).

Hespanha, J. P., Liberzon, D., and Morse, A. S. (2003). Hysteresis-based switching algorithms for supervisory control of uncertain systems. *Automatica*, 39(2):263–272.

Horn, R. A. and Johnson, C. R. (1985). *Matrix Analysis*. Cambridge University Press.

IMCA (2000). *IMCA M 140 Rev 1: Specification for DP capability plots*. International Marine Contractors Association.

Jenssen, N. A. and Realfsen, B. (2006). Power optimal thruster allocation. In *Proc. Dynamic Positioning Conference*, Houston, USA.

Johansen, T., Fossen, T., and Berge, S. (2004). Constrained nonlinear control allocation with singularity avoidance using sequential quadratic programming. *Control Systems Technology, IEEE Transactions on*, 12(1):211 – 216.

Johansen, T. A. (2004). Optimizing nonlinear control allocation. In *Proceedings of 43rd IEEE Conference on Decision and Control*, page 3435—3440, Paradise Island, Bahamas.

Johansen, T. A., Fossen, T. I., and Tøndel., P. (2005). Efficient optimal constrained control allocation via multiparametric programming. *Journal of Guidance, Control and Dynamics*, 28(3):506 – 515.

Johansen, T. A., Fuglseth, T. P., Tøndel, P., and Fossen, T. I. (2003). Optimal contrained control allocation in marine surface vessels with rudder. In *In Proceedings of 6th Conference on Manoeuvering and Control of Marine Crafts*, Girona, Spain.

Johansen, T. A., Fuglseth, T. P., Tøndel, P., and Fossen, T. I. (2008). Optimal constrained control allocation in marine surface vessels with rudders. *Control Engineering Practice*, 16(4):457 – 464. Special Section on Manoeuvering and Control of Marine Craft.

Johansen, T. A., Fuglseth, T. P., Tøndel, P. T., and Fossen, T. I. (2007). Optimal con-strained control allocation in marine surface vessels with rudders. *Control Engineering Practice*.

J.P. Shi, W.G. Zhang, G. L. and Liu, X. (2010). Research on allocation efficiency of the redistributed pseudo inverse algorithm. *Science China Information Sciences*, 53:271–277.

Khalil, H. (2002). *Nonlinear Systems*. Prentice Hall, Upper Saddle River, New Jersey, 3rd edition.

Koushan, K. (2006). Dynamics of ventilated propeller blade loading on thrusters. *World Maritime Technology Conferance*.

Liang, C. C. and Cheng, W. H. (2004). The optimum control of thruster system for dynamically positioned vessels. *Ocean Engineering*, 31(1):97–110.

Lindegaard, K. P. and Fossen, T. I. (2003). Fuel-efficient rudder and propeller control allocation for marine craft: Experiments with a model ship. *IEEE Trans. Control Systems Technology*, 11(6):850–862.

Lindfors, I. (1993). Thrust allocation method for the dynamic positioning system. *10th International Ship Control Systems Sympsosium (SCSS'93)*.

MCLab (2012). Marine cybernetics labratory. `http://www.ntnu.no/imt/lab/kybernetikk`.

MSSToolbox (2012). Marine systems simulator. `http://www.marinecontrol.org/`.

Myrhaug, D. (1993). *Irregular seas*. Cambridge University Press, Cambridge New York.

Nguyen, T. D., Sørensen, A., and Quek, S. T. (2008). Multi-operational controller structure for station keeping and transit operations of marine vessels. *Control Systems Technology, IEEE Transactions on*, 16(3):491 –498.

Nguyen, T. D., Sørensen, A. J., and Quek, S. T. (2007). Design of hybrid controller for dynamic positioning from calm to extreme sea conditions. *Automatica*, 43(5):768 – 785.

Nocedal, J. and Wright, S. J. (2006). *Numerical Optimization*. Springer, 2nd edition.

Oosterveld, M. and Ossanen, P. V. (1975). Further computer-analyzed data of the wageningen b-screw series. *Int. Shipbuilding Progress*, 22(251).

OpalRT (2012). Rt-lab professional. `http://www.opal-rt.com/product/rt-lab-professional`.

Oppenheimer, M., Doman, D., and Bolender, M. (2010). *The Control Handbook, Control System Applications*. CRC Press, second edition.

Petersen, J. A. M. and Bodson, M. (2006). Constrained quadratic programming techniques for control allocation. *IEEE Trans. Control Systems Technology*, 14:91–98.

Qualisys (2012). Qualisys position system. `http://www.qualisys.com/`.

Ruth, E. (2008). *Propulsion control and thrust allocation on marine vessels*. PhD thesis, Norwegian University of Science and Technology, Department of Marine Technology.

Ruth, E., Smogeli, O., Perez, T., and Sorensen, A. (2009). Antispin thrust allocation for marine vessels. *Control Systems Technology, IEEE Transactions on*, 17(6):1257–1269.

Ruth, E. and Sørensen, A. J. (2009). A solution to the nonconvex linearly constrained quadrating thrust allocation problem. In *Proceedings of 8th Conference on Manoeuvring and Control of Marine Craft*, page 195–200, Guaruj, Brazil.

Ruth, E., Sørensen, A. J., and Perez, T. (2007). Thrust allocation with linear constrained quadratic cost function. In *Conference on Control Applications in Marine Systems*, Bol, Croatia.

Schittkowski, K. (1986). A fortran code for quadratic programming. technical report. Technical report.

Sinding, P. and Anderson, S. V. (1999). A force allocation strategy for

dynamic positioning. In *Proceedings of the Eight International Offshore and Polar Engineering Conference*, page 346—353, Montreal, Canada.

SNAME (1950). *Nomenclature for Treating the Motion of a Submerged Body Through a Fluid*. The Society of Naval Architects and Marine Engineers.

Snell, S. A., Enns, D. F., and Garrard, W. L. (1990). Nonlinear inversion flight control for a supermaneuverable aircraft. In *AIAA Conference*, pages AIAA Paper 90–3406.

Sørdalen, O. J. (1996). Thrust allocation: Singularities and filtering. *13th World Congress of IFAC*, Q:369 – 374.

Sørdalen, O. J. (1997a). Full sea trials with optimal thrust allocation. *Preprints IFAC Conference on Maneuvering and Control of Marine Craft*, pages 177 – 182.

Sørdalen, O. J. (1997b). Optimal thrust allocation for marine vessels. *Control Engineering Practice*, 5(9):1223 – 1231.

Sørensen, A. (2003). Exam in course sin1549 marine control systems.

Sørensen, A. J. (2011). *Marine Control Systems: Propulsion and Motion Control of Ships and Ocean Structures*. Marine Technology Centre, Trondheim.

Sørensen, A. J. and Adnanes, A. K. (1997). High performance thrust allocation scheme in positioning of ships based on power and torque control. page 195–200.

Swanson, T. L. (1982). A generalized propulsion control logic. *IEEE International Conference on Engineering in the Ocean Environment*, pages 723–727.

T. A. Johansen, T. I. F. and Berge, S. P. (2004). Constrained nonlinear control allocation with singularity avoidance using sequential quadratic programming. *IEEE Trans. Control Systems Technology*, 12:211–216.

Tjønnås, J. and Johansen, T. A. (2005). Optimizing nonlinear adaptive control allocation. In *IFAC World Congress*, Prague, Czech Republic.

Tjønnås, J. and Johansen, T. A. (2007). On optimizing nonlinear adaptive

control allocation with actuator dynamics. In *7th IFAC Symposium on Nonlinear Control Systems*, Pretoria, South Africa.

van Lammeren, W., van Manen, J. D., and Oosterveld, M. (1969). The wageningen b-screw series. *Transactions of SNAME*, (8).

Virnig, J. and Bodden, D. (1994). Multivariable control allocation and control law conditioning when control effectors limit. In *Proc. AIAA Guidance, Navigation and Control Conf., Scottsdale, AZ*, pages AIAA 94–3609.

Webster, W. C. and Sousa, J. (1999). Optimum allocation for multriple thrusters. In *Proc. International Society of Offshore and Polar Engineers Conference*, Brest, France.

Øyvind N. Smogeli, Sørensen, A. J., and Minsaas, K. J. (2008). The concept of anti-spin thruster control. *Control Engineering Practice*, 16(4):465 – 481.

Appendix A

Background materials

A.1 Vessel equations

A.2 Marine vessel equations

In this paper the vectorial representation for marine crafts from Fossen (2011) has been used. The vectorial representation is

$$\boldsymbol{M}\dot{\boldsymbol{\nu}} + \boldsymbol{C}(\boldsymbol{\nu})\boldsymbol{\nu} + \boldsymbol{D}(\boldsymbol{\nu})\boldsymbol{\nu} + \boldsymbol{g}(\boldsymbol{\eta}) + \boldsymbol{g}_0 = \boldsymbol{\tau} + \boldsymbol{\tau}_{wind} + \boldsymbol{\tau}_{wave} \tag{A.1}$$

where the 6 degrees of freedom is

$$\boldsymbol{\eta} = [x,\ y,\ z,\ \phi,\ \theta,\ \psi]^T \tag{A.2}$$

$$\boldsymbol{\nu} = [u,\ v,\ w,\ p,\ q,\ r]^T \tag{A.3}$$

by the SNAME (1950)-convention. The matrices $\boldsymbol{M}$, $\boldsymbol{C}$ and $\boldsymbol{D}$ denote intertia, Coriolis and damping respectively. $\boldsymbol{g}(\boldsymbol{\eta})$ is the dynamic restoring forces such as gravitational and buoyancy forces, and $\boldsymbol{g}_0$ the static restoring forces.

A.2.1 Degrees of freedom

Degrees of freedom are motion variables, for marine crafts these are defined by SNAME (1950); surge, sway, yaw, roll, pitch and yaw. The forces, moments, velocities and position notation is described in Table A.1

Degree of Freedom	Linear Velocities	Position	Forces
1 - surge motion	u	x	X
2 - yaw motion	v	y	Y
3 - heave motion	w	w	Z
-	Angular Velocities	Euler Angels	Moments
4 - roll rotaion	p	ϕ	K
5 - pitch rotaion	q	θ	M
6 - yaw rotations	r	ψ	N

Table A.1: Marine Vessel notation from SNAME (1950)

A.2.2 Reference frames

When talking about reference frames it is important to note that Newton's second law only applies in an intertial frame. The only real inertial reference frame is in the center of the universe. All measurements done by Intertial Measurement units (IMU), Vertical Reference Unit (VRU) is done in a inertial reference frame, and these types of measurements are normally of no use to the user and thus need to be compensated for the rotation of the user specific references frame. The compensation is normally done in the measurement unit, and is in normal conditions not a worry for the user. All coordinate reference frames follow the right hand rule

When talking about reference frames used in marine applications the most common reference frames is the following, Fossen (2011):

- **ECI**

  The Earth Centered Inertial frame is an assumed inertial frame

(As earth or the solarsystem are not in a intertial space). Earth does not rotate in this reference frame. The Earth model is normally the World Geodetic System 1984 (WGS'84) described in Forssell (2008) and are used in Navstar GPS systems.

- **ECEF**

  Earth-centered Earth-fixed frame rotates along the z-axis of the ECI-frame with earth's rotation.

- **NED**

  North-East-Down frame is a local frame. The frame is found by taking the tangent of the earth's crust at a local longitude and latitude relative to the ECEF reference frame. X-axis points towards the magnetic North, y-axis to the east and z-axis downwards normal to the earth's crust. For maritime operations locally, at an almost constant longitude and latitude, this reference frame can be assumed to be inertial.

- **BODY**

  Body frame is a coordinate system with the origin located normally at the midship in the water line. The x-axis is directed from the aft to the fore, y-axis to starboard and z-axis pointing downwards. The position of the marine craft is described in the inertial frame, while the velocities (linear and angular) are described in the body-frame.

A.3 Propeller characteristics

A.3.1 Propeller dynamics and efficiency

When talking about propeller dynamics and efficiency it is important to define the operation quadrants for the propellers. The operation quadrants can be defined from the hydrodynamic pitch angle as in van

Lammeren et al. (1969). The hydrodynamic pitch angle is found by

$$\beta = arctan(\frac{V_a}{0.7\pi nD}) = arctan(\frac{V_a}{0.7\omega R}) \tag{A.4}$$

where V_a is the inflow velocity to the propeller. n and ω is the shaft speed in $[rps]$ and $[rad/s]$ respectively, and D is the propeller diameter. We can then define the operation quadrants as follows

Quadrant	Angles	Advance velocity	Shaft speed [rps]
1^{st}	$0° \leq \beta \leq 90°$	$V_a \geq 0$	$n \geq 0$
2^{nd}	$90° < \beta \leq 180°$	$V_a \geq 0$	$n < 0$
3^{rd}	$-180° < \beta \leq -90°$	$V_a < 0$	$n < 0$
4^{th}	$-90° < \beta < 0°$	$V_a < 0$	$n \geq 0$

Table A.2: Operation quadrants

Typical propeller models are described in either 1^{st} quadrant, $1^{st} + 4^{th}$ quadrants or all four quadrants depending on the modeling at hand. 1^{st} quadrant models is often used in the case of modeling thrusters where the ship is in transit, in which both the inflow velocity and shaft speed is positive. For azimuth thruster and pods it takes longer time to reverse the shaft speed than to rotate the thrusters and in these cases it is often enough to only consider $1^{st} + 4^{th}$ quadrants models, and is used in this paper. For complete thruster dynamics all the quadrants should be considered.

The propeller dynamics is experimental derived, and is often described by open water propeller characteristics. Conventional open water propeller characteristics are described by the thrust and torque coefficients K_T and K_Q. In Carlton (1994) the thrust and torque is defined as

$$T_p = \text{sign}(n)\rho K_T(J_a)n^2D^4 \tag{A.5}$$

$$Q_p = \text{sign}(n)\rho K_Q(J_a)n^2D^5 \tag{A.6}$$

and power as

$$P_p = 2\pi nQ_p = \text{sign}(n)2\pi\rho K_Q(J_a)n^3D^5 \tag{A.7}$$

where

T_p — propeller thrust

Q_p — propeller torque

P_p — propeller power

ρ — fluid density

n — propeller speed in rps (rounds per second)

D — propeller diameter

J_a — advance ratio

Typical values for K_T and K_Q is shown in Figure A.1 below.

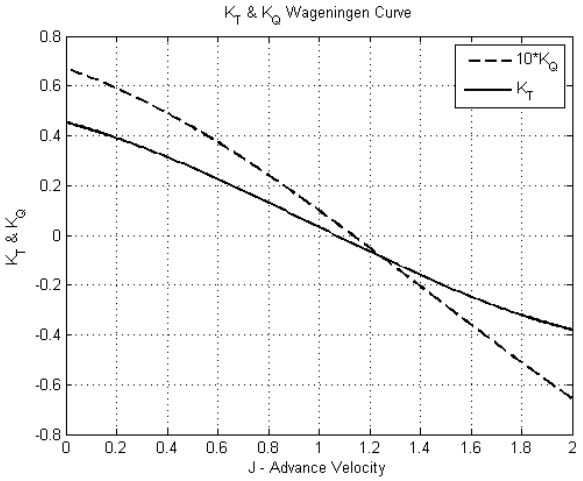

Figure A.1: Wageningen B-screw thruster series thrust and torque coefficient

The advance ratio is defined as follows

$$J_a := \frac{V_A}{nD} \tag{A.8}$$

where V_a is the inflow velocity to the propeller. One simple model for the inflow velocity is

$$V_a = U_r(1 - w_f) \tag{A.9}$$

defined in Carlton (1994) and where w_f is the wake fraction, typically in the range of $0 < w_f < 0.4$.

Extensive testing and model of Wageningen B-screw propellers series has been conducted in van Lammeren et al. (1969), Oosterveld and Ossanen (1975) and Bernitsas et al. (1981). These models are used a lot in the academic community.

One- and two quadrant model

The thrust and torque coefficients can be written as described in Oosterveld and Ossanen (1975)

$$K_T(J_a) = f_T(J_a, \frac{P}{D}, \frac{A_E}{A_O}, Z, Re, \frac{t}{c}) \tag{A.10}$$

$$K_Q(J_a) = f_Q(J_a, \frac{P}{D}, \frac{A_E}{A_O}, Z, Re, \frac{t}{c}) \tag{A.11}$$

$$\eta_0 = \frac{J_a}{2\pi}\frac{K_T}{K_Q} \tag{A.12}$$

where η_0 is the open water propeller efficiency.

The representation in Oosterveld and Ossanen (1975) of (A.10) and (A.11) was derived by multiple regression analysis

$$K_T = \sum_{s,t,u,v} C^T_{s,t,u,v} \cdot (J)^s (\frac{P}{D})^t (\frac{A_E}{A_O})^u (Z)^v \tag{A.13}$$

$$K_Q = \sum_{s,t,u,v} C^Q_{s,t,u,v} \cdot (J)^s (\frac{P}{D})^t (\frac{A_E}{A_O})^u (Z)^v \tag{A.14}$$

where the coefficients $C^T_{s,t,u,v}$ and $C^T_{s,t,u,v}$ for Reynolds numbers for 2×10^6 and above are given in Oosterveld and Ossanen (1975).

Four-Quadrant model

The thrust and torque can also be described by a four-quadrant model as in van Lammeren et al. (1969). This model relies on the hydrodynamic pitch angle.

The Thrust and Torque is here described by the nondmensional thrust and torque coefficients

$$C_T^* = \frac{T_a}{\frac{1}{2}\rho\left[V_a^2 + (0.7\pi nD)^2\right]\frac{\pi}{4}D^2} \tag{A.15}$$

$$C_Q^* = \frac{Q_a}{\frac{1}{2}\rho\left[V_a^2 + (0.7\pi nD)^2\right]\frac{\pi}{4}D^3} \tag{A.16}$$

where C_T^* and C_Q^* is approximated by Fourier series and not restated here. However it should be noted that the four quadrant data from van Lammeren et al. (1969) might be wrong. In Ruth (2008) a series of analysis were made on the Wageningen dataset, and it was found that while the data for one and two quadrant models were correct while for the four quadrant model the data were not sufficient. Due to this the four quadrant model in this thesis is not utilized.

A.3.2 Typical thrust losses on a supply vessel

Thrust losses is by definition the loss of produced force while drawing same amount of power. The specific thrust is defined as force divided by power, normally in either [N/W] or [kN/kW].

Common losses on thruster for a normal DP supply vessel is due to the Coanda effect, in-out-of-water effects, ventilation, thruster to thruster interaction, loss of propeller disk area, change of inflow velocity to the thruster and transverse water flow velocity.

The Coanda effect is, as described in Faltinsen (1993), an example of hull interaction effect. The slip stream from the thruster is attracted to the curved surface of the hull. And a consequence of this is loss of thruster

effect. The water stream is attracted to the hull due to the high velocity behind the thruster and the low velocity at the hull, and thus pressure differences drives the water stream upwards to the hull.

Ventilation is the case where the thruster is no longer deeply submerged and comes close to the free surface. This can cause a stream of air being sucked down towards the propeller and can cause serious loss of thrust forces, Faltinsen (1993). As stated in Koushan (2006) a ventilation incident can cause more than 40% loss in a well submerged thruster and approximately 90% loss in a partially submerged thruster.

Thruster to thruster interaction is often the case where one thrusters' wake field is in the direction of another thruster. This will decrease the thrusters' ability to accelerate the fluid particles and thus reduce its thrust production efficiency. As mentioned in Ekstrom and Brown (2002), if a thruster is operating in a slipstream of another thruster the reduction in thrust can be as much as 40%. This depends much on the distance between the different thrusters.

Appendix B

Cybership III Data

The CyberShip III data can be found in Parameters.m in the DVD with the simulation file MCSim.mdl. As the data for CyberShip III lies in different folders on the DVD, the easiest way to access them is to run the scrip in MCS.m and type edit to the file wanted to be found. MCS.m includes a description of the files. Thruster data can be found in the Thruster_config.m. The environmental data can be found in the file Thruster_data.m.

Hull	**Symbol**			
Model Scale	λ	30		
		Model	**Ship**	
Length over all	L_{oa}	2.275 m	68.28 m	
Length between perp.	L_{pp}	1.971 m	59.13 m	
Breath	B	0.437 m	13.11 m	
Draught	T (Lpp/2)	0.153 m	4.59 m	
Draught front perp.	T_{fp}	0.153 m	4.59 m	
Draught aft. perp.	T_{ap}	0.153 m	4.59 m	
Depth to main deck	D	0.203 m	6.10 m	
Weight (hull)	M_E	17.5 kg	Unknown	
Weight (normal load)	M	74,2 kg	2262 tons	
Longitudinal centre of gravity (from FP)	LCG (average load)	100 cm	30 m	
Vertical centre of gravity	CG (average load)	19.56 cm	5.87 m	
Propeller data		**Pod**	**Azimuth**	**Tunnel thruster**
Number of blades	Z	4	4	Displacement thruster
Diameter	D	9 cm	4 cm	2 cm
Boss diameter	r_0	1.4 cm	1 cm	–
Material thickness	t_0	0.12 cm	0.1 cm	–
Pitch angle (0.7D)	ϕ	20.11°	Unknown	–
Propeller disc area	A_0	62.62 cm^2	12.57 cm^2	3.14 cm^2
Projected blade area	A_p	31.5 cm^2	Unknown	–
Actual blade area	A	43.35 cm^2	Unknown	–
Blade area relation	EAR	0.6814	Unknown	–
Max. rotational speed	n_{max}	40 rps	80 rps	80 rps
Estimated thrust				
Max shaft power	P_{max_shaft}	33.8 W	33.8 W	33.8 W
Max Thrust (Bollard pull)	T_{max}	21.9 N	10 N	7 N
Min Thrust (Bollard pull)	T_{min}	-21.9 N	-10 N	-7 N
Thrust coefficient	$K_T(T/n^2)$	0.01369	0.00156	0.001094
Torque coefficient	$K_Q(Q/n^2)$	Unknown	Unknown	Unknown

Table B.1: Main particulars of Cybership III, found in Sørensen (2003)

Appendix C

Simulation Parameters

C.1 Supervisory Control Allocation

```
Control.Allocation.stepLength = 0.1;
nt = 3;
na = 3;
ns = 3;

%% QP Optimization configuration
%SuperVisor
Control.Allocation.Supervisor.T_lim = 5;
Control.Allocation.Supervisor.Plim = 0.4;
Control.Allocation.Supervisor.numSectors = 9;

Control.Allocation.Params.ly = [0, 0.123, -0.123];
Control.Allocation.Params.lx = [0.55, -0.875, -0.875];
Control.Allocation.Params.rhow = 1025;

%Precalculations:
Control.Allocation.Params.powerThrustRelation_Vec = [41...
    .9190; 1.5844; 1.5844];
Control.Allocation.Params.q = nt/(sum(...
    Control.Allocation.Params.powerThrustRelation_Vec));


```

```
% Cost Function
Control.Allocation.Params.W_u = zeros(nt,nt);
for i = 1:nt
    % Multiply by 2 due to QP solver notation
    Control.Allocation.Params.W_u(i,i) = 2*(...
        Control.Allocation.Params.q*...
        Control.Allocation.Params.powerThrustRelation_Vec(i...
        ,1));
end

Control.Allocation.Params.alpha_weight = 0.6;
Control.Allocation.Params.Omega_alpha = ...
    Control.Allocation.Params.alpha_weight.*eye(na,na);
Control.Allocation.Params.s_weight =  1000;
Control.Allocation.Params.Q_s = ...
    Control.Allocation.Params.s_weight.*eye(ns,ns);

%Singularity Variables
Control.Allocation.Params.Singularity.rho = 0.0;
Control.Allocation.Params.Singularity.eps = 1e-9;

% Equality Constraint
Control.Allocation.Params.lbA_eps = zeros(3,1);
Control.Allocation.Params.ubA_eps = zeros(3,1);


%Inequality Constraints: Eivind Ruth
Control.Allocation.Params.T_max = [7.33;21.9;21.9];
Control.Allocation.Params.T_min = [-7.33;0.00005;0.00005];
Control.Allocation.Params.Δ_T_max = 0.2.*...
    Control.Allocation.Params.T_max;
Control.Allocation.Params.Δ_T_min = -...
    Control.Allocation.Params.Δ_T_max;
Control.Allocation.Params.Δ_alpha_max = (1/...
    Control.Allocation.stepLength).*[90*pi/180; 1*pi/180; ...
    1*pi/180]';
Control.Allocation.Params.s_max = 1e9*ones(3,1);
Control.Allocation.Params.s_min = -...
    Control.Allocation.Params.s_max;
Control.Allocation.Params.c1 = 0.9;

%% Setup Superviosor Sector Solutions

%Sector 1
```

```
55      Control.Allocation.Params.SectorSolution{1}.alpha_max ...
            = (pi/180).*[90;70;109];
56      Control.Allocation.Params.SectorSolution{1}.alpha_min ...
            = (pi/180).*[90;-109;-70];
57
58  %Sector 2
59      Control.Allocation.Params.SectorSolution{2}.alpha_max ...
            = (pi/180).*[90;70;159];
60      Control.Allocation.Params.SectorSolution{2}.alpha_min ...
            = (pi/180).*[90;-109;-20];
61
62  %Sector 3
63      Control.Allocation.Params.SectorSolution{3}.alpha_max ...
            = (pi/180).*[90;70;-110];
64      Control.Allocation.Params.SectorSolution{3}.alpha_min ...
            = (pi/180).*[90;-109;-150];
65
66  %Sector 4
67      Control.Allocation.Params.SectorSolution{4}.alpha_max ...
            = (pi/180).*[90;20;109];
68      Control.Allocation.Params.SectorSolution{4}.alpha_min ...
            = (pi/180).*[90;-159;-70];
69
70  %Sector 5
71      Control.Allocation.Params.SectorSolution{5}.alpha_max ...
            = (pi/180).*[90;20;159];
72      Control.Allocation.Params.SectorSolution{5}.alpha_min ...
            = (pi/180).*[90;-159;-20];
73
74  %Sector 6
75      Control.Allocation.Params.SectorSolution{6}.alpha_max ...
            = (pi/180).*[90;20;-110];
76      Control.Allocation.Params.SectorSolution{6}.alpha_min ...
            = (pi/180).*[90;-159;-150];
77
78  %Sector 7
79      Control.Allocation.Params.SectorSolution{7}.alpha_max ...
            = (pi/180).*[90;150;109];
80      Control.Allocation.Params.SectorSolution{7}.alpha_min ...
            = (pi/180).*[90;110;-70];
81
82  %Sector 8
83      Control.Allocation.Params.SectorSolution{8}.alpha_max ...
            = (pi/180).*[90;150;159];
```

```
84      Control.Allocation.Params.SectorSolution{8}.alpha_min ...
            = (pi/180).*[90;110;-20];
85
86  %Sector 9
87      Control.Allocation.Params.SectorSolution{9}.alpha_max ...
            = (pi/180).*[90;150;-110];
88      Control.Allocation.Params.SectorSolution{9}.alpha_min ...
            = (pi/180).*[90;110;-150];
89
90  Control.Allocation.NumSectors = length(...
        Control.Allocation.Params.SectorSolution);
```

Appendix D

Simulation Study

This chapter contains the relative results from the simulation studies conducted in this thesis.

D.1 Simulation Case 2: S2

This section contains supplement results to the tests conducted in section 5.2.

D.1.1 Ppseudo-inverse control allocation results

The results of the Pseudo inverse of the simulation case in section 5.2, which are not added there, can be found in figures D.1- D.4

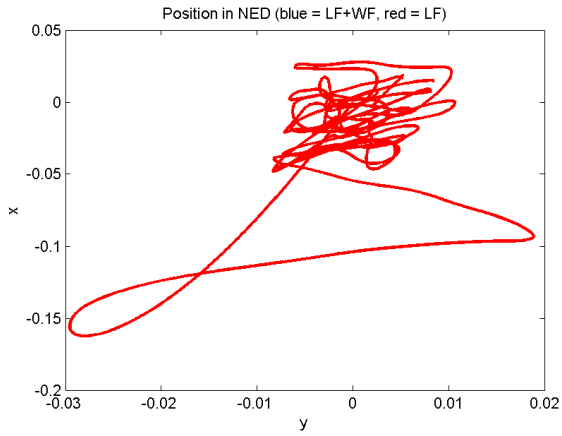

Figure D.1: Simulation Case 2 - Pseudo-Inverse: North-East position result

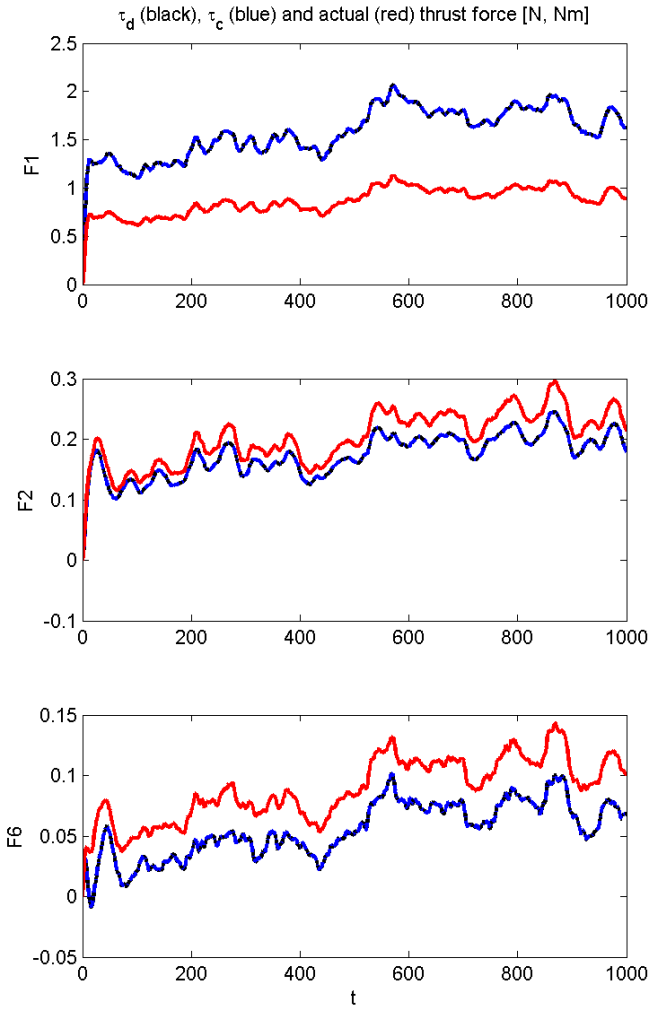

Figure D.2: Simulation Case 2 - Pseudo-Inverse: 3-DOF body-framed forces and moment

Environmental Loads

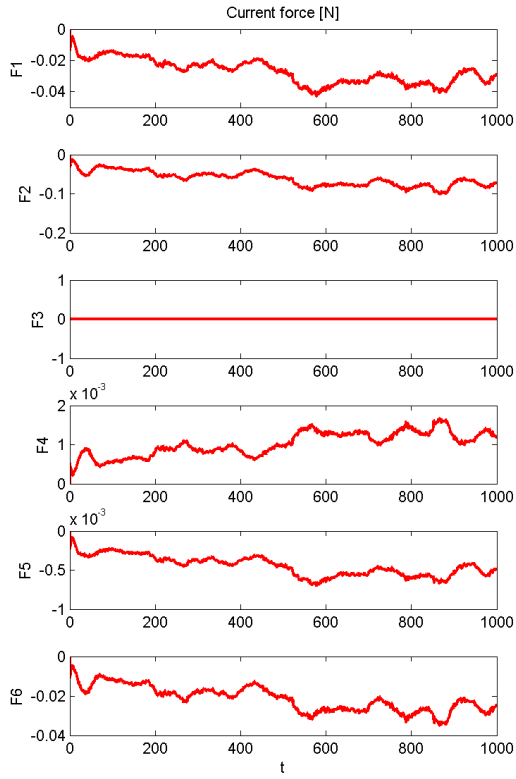

Figure D.3: Simulation Case 2 - Pseudo-Inverse: 6-DOF Current forces and moments

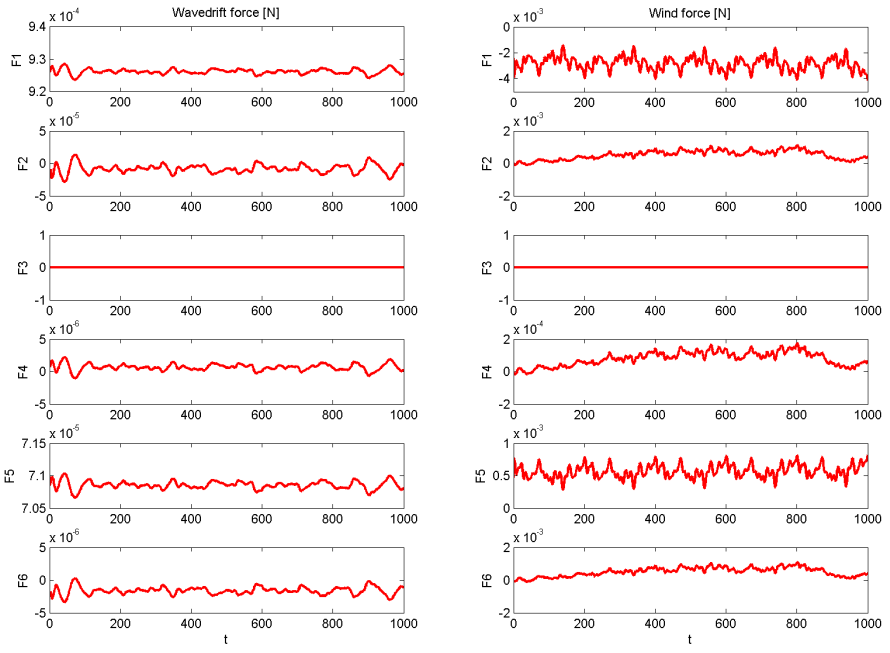

Figure D.4: Simulation Case 2 - Pseudo-Inverse: 6-DOF Wavedrift forces and moments (left) and Wind forces and moments (right)

D.1.2 Results of Supervisory Control Allocation

The results from the Supervisory Control Allocation conducted in the simulation study case in section 5.2, and not added there, can be found in the figures D.5- D.9

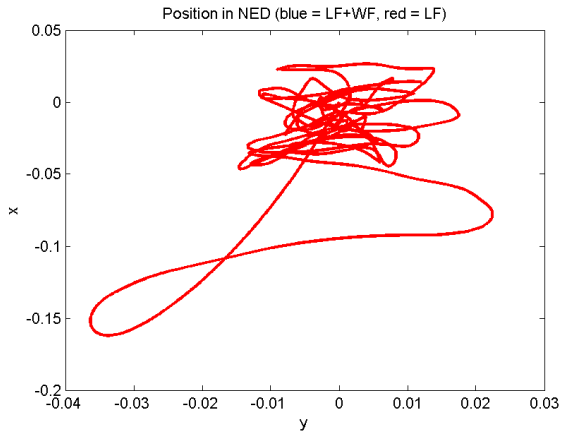

Figure D.5: Simulation Case 2 - Supervisory Control Allocation: North-East position result

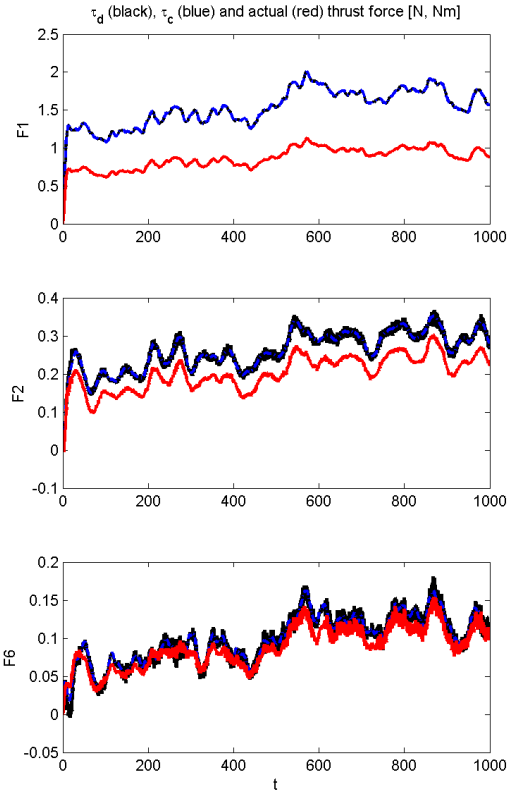

Figure D.6: Simulation Case 2 - Supervisory Control Allocation: 3-DOF body-framed forces and moments. Where desired, commanded and actual is denoted with black, blue and red colors respectively.

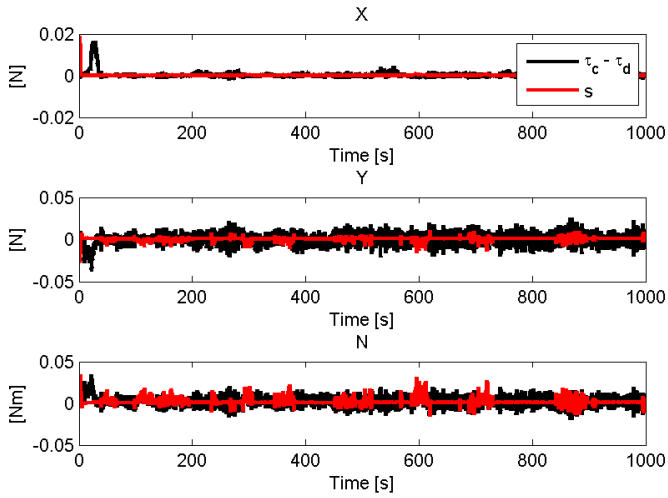

Figure D.7: Simulation Case 2 - Supervisory Control Allocation: Difference between commanded and desired generalized forces and moments (marked as black) and the linearized difference used by the allocation algorithm (marked as red).

Environmental Loads

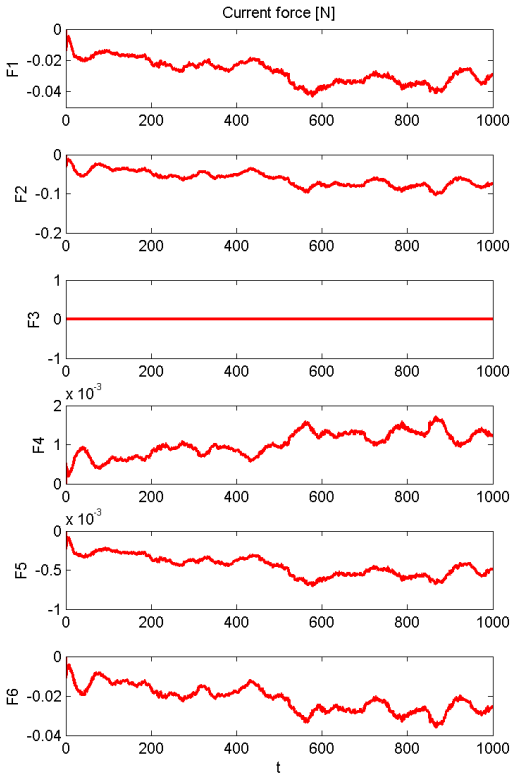

Figure D.8: Simulation Case 2 - Supervisory Control Allocation: 6-DOF Current forces and moments

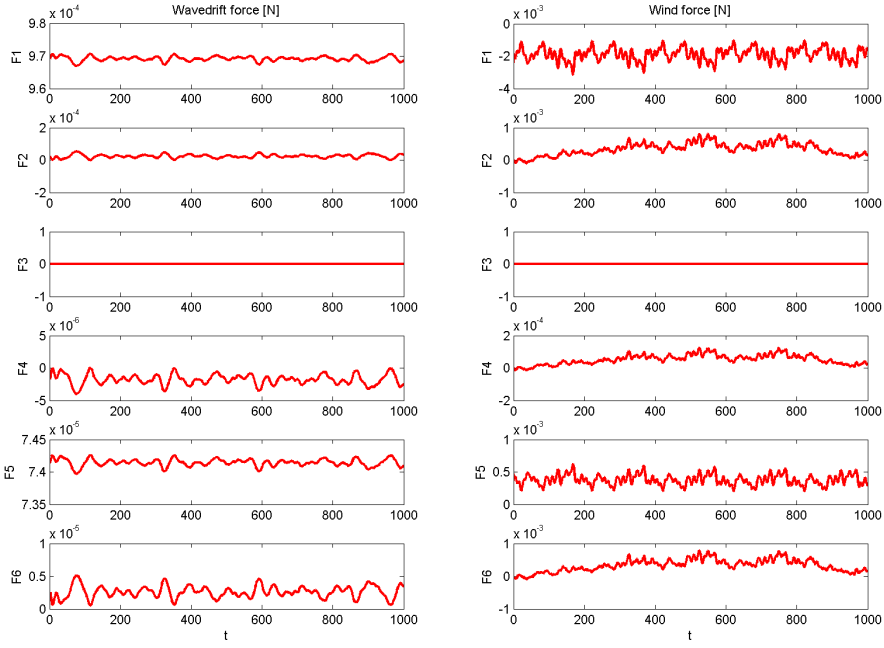

Figure D.9: Simulation Case 2 - Supervisory Control Allocation: 6-DOF Wavedrift forces and moments (left) and Wind forces and moments (right)

Appendix E

DVD content

The content of the DVD is splitted into two folders. SimulationTesting and ExperimentalTesting.

In the SimulationTesting 3 subfolders are added

- CompareTinvAndAlloc
  - This folder includes the simulation tests for the Simulation Case 2: CS3-SupervisoryControlAllocation includes the files for the simulation for the supervisory control allocation. CS3-Tinv includes the files for the simulation of the pseudo-inverse control allocation. For both folders the results are in the Results folder.
- ConstantTauTesting
  - This folder includes the figures for the Simulation Case 1
- SingularityAvoidanceTesting
  - This folder includes the simulation tests for Simulation Case 3. The results are in the Results folder.

For the folders CS3-SupervisoryControlAllocation, CS3-Tinv, and SingularityAvoidanceTesting the results are in the Results folder. The supervisory control allocation parameters with both the parameters and

the c-code to run the allocation algorithm is in the folder KjellErikLarsen. The main c-code file that is run in the Simulink file MCSim.mdl is the qpSolverAlpha.c. This file calls qpSolverAlpha_wrapper.c which breaks up the matrices in the supervisory control allocation algorithm and sends it to qld.c to be solved. To run any simulations the MCS.m is called first to load all the relative paths to the CyberShip III m-files. After the loading is complete run Init.m to initialize the parameters, and then the simulation can start by opening MCSim.mdl and press play. The vessel_data can be found under the Vessel_data folder and in the file MC_CS3_1.m file. Control data is found in Controls.m. While the thruster data is in Thruster_config.m. To plot results a call to the plotResults.m will call most of the processing files under the folder Process folder.

In the ExperimentalTesting folder the logged mat files for the experimental study is found in the folder Mat-files. The figures for these mat files are found in the Results folder.